Computers & Fluids 74 (2013) 13–31

Contents lists available at SciVerse ScienceDirect

Computers & Fluids

journal homepage: www.elsevier.com/locate/compfluid

Numerical study of two regularization models for simulating the turbulent flows

Tony W.H. Sheu [a,b,c,*], Y.X. Lin [a], C.H. Yu [a]

[a] Department of Engineering Science and Ocean Engineering, National Taiwan University, No. 1, Section 4, Roosevelt Road, Taipei, Taiwan, ROC
[b] Department of Mathematics, National Taiwan University, No. 1, Section 4, Roosevelt Road, Taipei, Taiwan, ROC
[c] Center of Advanced Study in Theoretical Sciences (CASTS), National Taiwan University, Taiwan, ROC

ARTICLE INFO

Article history:
Received 22 March 2012
Received in revised form 25 October 2012
Accepted 8 December 2012
Available online 11 January 2013

Keywords:
Regularization models
Turbulent
Leray-α
NS-α
Subgrid scale

ABSTRACT

In this study two previously proposed regularization models employed for simulating turbulent fluid flows in large-eddy template are numerically assessed. Both of the Leray-α and NS-α subgrid scale models are under current investigation. For an accurate assessment of these differential models developed on the basis of regularizing the nonlinear convective terms, a dispersively very accurate upwinding scheme is proposed to approximate the regularized convective terms in non-staggered grids. These models are assessed through the calculation of the lid-driven cavity and backward facing step problems. We conclude from this study that application of the NS-α model can get a solution having a better agreement with the classical Navier–Stokes solution which is computed in a four-time finer grids.

© 2012 Elsevier Ltd. All rights reserved.

1. Introduction

Transport phenomena in nature and many processing industries are normally characterized to be turbulent. Since flow turbulence has association with a broad dynamical range of time and length scales, complex multiscale dynamics can be observed very often in a wide variety of flows. As a result, to get an accurately predicted turbulent flow one should model its associated nonlinear interaction physics among the physically different lengths. Take an incompressible viscous fluid flow as an example, the solutions to the corresponding set of equations have different ranges of length that can extend to a scale as small as the Kolmogorov dissipation scale, which is proportional to the Reynolds number Re in a sense of $Re^{-\frac{3}{4}}$ [1]. At $Re = 10^7$, for example, any flow simulation carried out at this Reynolds number requires a dimensionless mesh size not larger than 5.62×10^{-6} in order to properly resolve most of the flow details numerically. Such a fine-mesh calculation performed in a three-dimensional domain poses a severe computational difficulty and motivated, thus, many previous studies aiming at coping with such a simulation difficulty.

One of the possible ways of overcoming the numerical difficulty about the multiscale nature of the turbulent flow is to resolve only the primary flow features. Instead of performing a direct numerical simulation (DNS) on the incompressible Navier–Stokes equations, in this study the concept based on the restriction of flow equations is adopted so that the computational effort can be considerably reduced. Hence it is feasible to carry out flow simulations, for which their Reynolds numbers falling into the turbulent range, in many currently available computing infrastructures.

The equations of motion for an incompressible fluid flow contain the linear spatial derivative term $\nabla^2 \underline{u}$, which is effective mostly at the smallest scale motion, and the nonlinear term $\underline{u} \cdot \nabla \underline{u}$. Unlike the dissipative nature exhibited in the linear term $\nabla^2 \underline{u}$, the convective term transfers the energy of fluid flow from a scale at which the flow is driven to the smallest one that survives dissipation [2]. This implies that $\underline{u} \cdot \nabla \underline{u}$ can in principle produce an infinite number of scales of flow motion. As a result, one requires modeling all the dynamical scales of flow motion for getting a truly accurate turbulent flow solution.

According to the book of Pope [3], one can get a sufficiently accurate mean flow if eighty percentage of the total kinetic energy can be predicted numerically. In this light, most of the energy contained in a flow can be simply represented by its primary flow feature [4]. Simulation of the viscous flow equations, as a result, needs not necessarily to take all the dynamical scales up to the Kolmogorov dissipative scale into consideration. In other words, one can simply apply a dynamically less complex Large Eddy Simulation (LES) model to simulate the transport of flow turbulence.

On a coarse grid, one needs only to resolve the energy-containing large scale motion. The unresolved turbulent flow motion and the molecular diffusion effect can be modeled by adding an explicit

* Corresponding author at: Department of Engineering Science and Ocean Engineering, National Taiwan University, No. 1, Section 4, Roosevelt Road, Taipei, Taiwan, ROC. Tel.: +886 2 33665746; fax: +886 2 23929885.
E-mail address: twhsheu@ntu.edu.tw (T.W.H. Sheu).

0045-7930/$ - see front matter © 2012 Elsevier Ltd. All rights reserved.
http://dx.doi.org/10.1016/j.compfluid.2012.12.010

subgrid scale viscosity damping in coarse grids to modify the dissipative processes [5]. The other major class of approaches is referred to as the regularization method. Unlike the closures of eddy viscosity type developed to modify the dissipative processes, regularization model modifies the spectral distribution of the energy [6]. When employing the regularization strategy to account for the subgrid-scale contribution, it is desired to preserve some physical constraints. Conservation of energy and helicity and preservation of Kelvin's circulation are often referred to [5]. In a context of LES, a spatial filtering of the Navier–Stokes equations can be made through the length-scale that is larger than the Kolmogorov dissipation scale. Such an explicit filtering of the equations, while providing us a good control over the effective dynamical range of the smoothed flow, has a demand for the so-called sub-filter models so as to approximate more accurately the dynamical issues of smaller scales for an evolution of the resolved large scale [4].

Besides the Smagorinsky's eddy viscosity model [7], another scale-similarity Bardina's model [8] developed on the basis of adding a dissipative flux term to the differential system has been proposed before. In the context of sub-filter models, regularization models have been developed by making a direct modification of the convective flux terms in the equations. Two regularization models are chosen in this study to simulate flow turbulence. Our aim is to numerically assess two regularization models, which differ from each other by the way of filtering the convected fluxes in the Navier–Stokes equations. Through the use of their own regularization kernels, one can directly regularize the convective terms to yield $\frac{\partial}{\partial x_j}(v_j w_i)$, where $\underline{v}$ and $\underline{w}$ are referred to as the convecting velocity vector and the convected velocity vector, respectively [4].

In this study our previously proposed dispersively very accurate advection scheme will be applied to simulate the incompressible fluid flow using two sub-grid models. Our aim is to assess these regularization models by comparing the predicted results with the direct Navier–Stokes results computed in a much finer grid system. The rest of this article is organized as follows. We start with the presentation of the Navier–Stokes equations and their regularized equations for the nonlinear convective terms. In Section 3, the proposed advection scheme that can rigorously optimize the dispersion nature in wavenumber space will be briefly described. The incompressible Navier–Stokes flow solver developed in non-staggered grids will be adopted to avoid the even–odd decoupling pressure mode. In Section 5 we describe the model problem and present the numerical details. The results computed from the investigated regularized Navier–Stokes equations will then be compared with the DNS solutions so as to be able to make an assessment of the two investigated sub-grid turbulence models. Finally, some conclusions will be drawn in Section 6 based on the simulated results for the chosen lid-driven cavity and backward facing step problems.

2. Governing equations

In this numerical study a fluid flow of constant density is considered. The conservation equations for mass and momenta are expressed in terms of the primitive variables $\underline{u}$ (flow velocity vector) and p (pressure)

$$\nabla \cdot \underline{u} = 0, \tag{1}$$

$$\underline{u}_t + \underline{u} \cdot \nabla \underline{u} = -\nabla p + \frac{1}{Re}\nabla^2 \underline{u}. \tag{2}$$

The dynamical control parameter for the above elliptic–parabolic set of partial differential equations is the Reynolds number Re. This characteristic number is defined by the kinematic fluid viscosity v and the referenced velocity and length as $Re = \frac{u_{ref} l_{ref}}{v}$.

In the filtering approach, a proper convolution filter L is chosen to model flow turbulence. In the context of large-eddy simulation, the velocity vector $\underline{u}$ is filtered to get its filtered velocity vector counterpart $\overline{\underline{u}}$ through the transformation given by $\overline{\underline{u}}(\underline{x}, t) = L(\underline{u})(\equiv \int_{-\infty}^{\infty} G(\underline{x} - \underline{\xi})\underline{u}(\underline{\xi}, t)d\underline{\xi})$. Different filters are characterized by their own kernels and filter widths. In the current large eddy simulation study, the adopted convolution filter is the inverse of the well-known Helmholtz filter, which is defined as $H = (1 - \alpha^2\nabla^2)$. Hence one can transform the unfiltered velocity vector $\underline{u}$ to the filtered velocity vector $\bar{\underline{u}}$ through the elliptic Helmholtz operator to yield $\underline{u} = (1 - \alpha^2\nabla^2)\bar{\underline{u}}$. The filtered velocity vector can be therefore expressed in terms of the unfiltered velocity vector as $\bar{\underline{u}} = (1 - \alpha^2\nabla^2)^{-1}\underline{u}$, where $(1 - \alpha^2\nabla^2)^{-1}$ denotes the smoothing operator. The users' specified parameter α shown in the Helmholtz filter denotes the effective width of the chosen filter. Such a filter corresponds to the length scale at which smoothing becomes essential.

When filtering the NS Eqs. (1) and (2), low-pass spatial filter is required [9]. Given a convolution filter having its own formal inverse, in this paper two regularization strategies for the subgrid closure are employed and numerically assessed. They are known as the Leray-α and Lagrangian Averaging Navier–Stokes-α (LANS-α) regularization approaches. The subgrid models under current investigation have a sharp contrast to the traditional phenomenological subgrid modeling, by which the fluid flow is smoothed by the introduced subgrid model for the turbulent stress components.

2.1. Leray-α model equations

The Leray-α model is the simplest one belonging to the class of regularization models. This model involves using the inverse-Helmholtz operator of width α to directly and explicitly replace the nonlinear advective term $\underline{u} \cdot \nabla \underline{u}$ with the linearized term $\overline{\underline{u}} \cdot \nabla \underline{u}$. The filtered velocity vector $\overline{\underline{u}}$ results from the application of the Helmholtz filter H $(\equiv (1 - \alpha^2\nabla^2))$ to the velocity, thus yielding

$$\overline{\underline{u}} = H^{-1}(\underline{u}). \tag{3}$$

Upon applying the Helmholtz filter to the Navier–Stokes Eqs. (1) and (2), the Leray-α equations are derived below [10]

$$(I - \alpha^2\nabla^2)\overline{\underline{u}} = \underline{u}, \tag{4}$$

$$\underline{u}_t + \overline{\underline{u}} \cdot \nabla \underline{u} = -\nabla p + \frac{1}{Re}\nabla^2 \underline{u}, \tag{5}$$

Table 1
Summary of the Leray-α model equations.

	Original form in the paper	Current form
(1)	$\partial_t v - v\Delta v + (u \cdot \nabla)v = -\nabla p + f$, $\nabla \cdot u = \nabla \cdot v = 0$, $v = u - \alpha^2 \Delta u$. [27]	$\frac{\partial \underline{U}}{\partial t} + (\overline{\underline{U}} \cdot \nabla)\underline{U} = -\nabla p + v\nabla^2 \underline{U} + \underline{f}$, $\nabla \cdot \underline{U} = \nabla \cdot \overline{\underline{U}} = 0$, $(I - \alpha^2\nabla^2)\overline{\underline{U}} = \underline{U}$.
	$\partial_t v - v\Delta v + (u \cdot \nabla)v = -\nabla p + f$ $\nabla \cdot u = \nabla \cdot v = 0$, $v = (I - \alpha^2\Delta)u$. [28]	
(2)	$\frac{\partial}{\partial t} v - v\Delta v + (u \cdot \nabla)v + \nabla p = f$, $\nabla \cdot v = 0$, [10] $v = u - \alpha^2 \Delta u$.	$\frac{\partial \underline{U}}{\partial t} + (\overline{\underline{U}} \cdot \nabla)\underline{U} = -\nabla p + v\nabla^2 \underline{U} + \underline{f}$, $\nabla \cdot \underline{U} = 0$, $(I - \alpha^2\nabla^2)\overline{\underline{U}} = \underline{U}$.
	$\partial_t u_i + \bar{u}_j \partial_j u_i = v\partial_j^2 u_i - \partial_i p + f_i$, $\partial_i u_i = 0$, [29] $(1 - \partial_j \alpha_j^2 \partial_j)\bar{u}_i = u_i$.	
(3)	$\partial_t u + \bar{u} \cdot \nabla u + \nabla p - v\nabla^2 u = \bar{f}$, [13] $\nabla \cdot u = 0$.	$\frac{\partial \underline{U}}{\partial t} + (\overline{\underline{U}} \cdot \nabla)\underline{U} = -\nabla p + v\nabla^2 \underline{U} + \underline{f}$, $\nabla \cdot \underline{U} = 0$.
	$\omega_t + \overline{\omega} \cdot \nabla \omega + \nabla q = v\Delta\omega + f$, [26] $\nabla \cdot \omega = 0$.	
	$u_t + \bar{u} \cdot \nabla u + \nabla q - v\Delta u = f$, [30] $\nabla \cdot u = 0$.	

$$\nabla \cdot \underline{u} = 0. \tag{6}$$

The resulting nonlinear effect is known to be reduced by an amount governed by the Helmholtz filtering operation.

The above set of Leray-α equations has relation to the LES equations derived from a completely different principle. In the LES template, the recast equations contain the turbulent stress tensor $\overline{\overline{u_j}u_i} - \overline{u_j}\overline{u_i}$. Note that the subgrid stress tensor in the Clark-α model equations is the truncated subgrid stress tensor in the Leray-α model equations [11]. The solution corresponding to the asymmetric Leray-α model possesses the global existence, uniqueness, and boundedness mathematical properties [9].

Table 2
Summary of the Navier–Stokes-α model equations.

	Original form in the paper	Current form
(1)	$\frac{\partial v}{\partial t} + v(-\Delta)^{\theta_2} v - u \times (\nabla \times v) + \nabla p = f$, $\nabla \cdot u = 0, \nabla \cdot v = 0$, $v = u + (-\alpha^2\Delta)^{\theta_1} u$, when $\theta_1 = \theta_2 = 1$. [25]	$\frac{\partial \underline{U}}{\partial t} - \underline{\overline{U}} \times (\nabla \times \underline{U}) = -\nabla p + \nu\nabla^2 \underline{U} + \underline{f}$, $\nabla \cdot \underline{U} = \nabla \cdot \underline{\overline{U}} = 0$, $(I - \alpha^2\nabla^2)\underline{\overline{U}} = \underline{U}$.
	$\partial_t \tilde{v} - \nu\Delta\tilde{v} - \tilde{u} \times \nabla \times \tilde{v} = -\nabla\tilde{p} + f$, $\nabla \cdot \tilde{u} = \nabla \cdot \tilde{v} = 0$, $\tilde{v} = (I - \alpha^2\Delta)\tilde{u}$. [26]	
(2)	$u_t - \overline{u} \times (\nabla \times u) + \nabla q - \nu\Delta u = f$, $\nabla \cdot \overline{u} = 0$, $-\alpha^2\Delta\overline{u} + \overline{u} = u$, $q = p + \frac{1}{2}u^2$. [30]	$\frac{\partial \underline{U}}{\partial t} - \underline{\overline{U}} \times (\nabla \times \underline{U}) = -\nabla\overline{p} + \nu\nabla^2 \underline{U} + \underline{f}$, $\nabla \cdot \underline{\overline{U}} = 0, (I - \alpha^2\nabla^2)\underline{\overline{U}} = \underline{U}$, $\overline{p} = p + \frac{1}{2}\lvert\underline{U}\rvert^2$.
(3)	$v_t - \overline{v} \times (\nabla \times v) + \nabla\tilde{p} = \nu\Delta v + f$, $\nabla \cdot \overline{v} = 0$. [28]	$\frac{\partial \underline{U}}{\partial t} - \underline{\overline{U}} \times (\nabla \times \underline{U}) = -\nabla p + \nu\nabla^2 \underline{U} + \underline{f}$, $\nabla \cdot \underline{\overline{U}} = 0$.
(4)	$\partial_t u + (\nabla \times u) \times \overline{u} + \nabla\pi - \nu\nabla^2 u = \overline{f}$, $\nabla \cdot u = 0$, $\pi = p + \frac{1}{2}u^2$. [13]	$\frac{\partial \underline{U}}{\partial t} + (\nabla \times \underline{U}) \times \underline{\overline{U}} = -\nabla\overline{p} + \nu\nabla^2 \underline{U} + \underline{f}$, $\nabla \cdot \underline{U} = 0, \overline{p} = p + \frac{1}{2}\lvert\underline{U}\rvert^2$.
(5)	$v_t + \overline{v} \cdot \nabla v + (\nabla\overline{v})^T \cdot v + \nabla p = \nu\Delta v + f$, $\nabla \cdot \overline{v} = 0$, $\overline{v} = (-\alpha^2\Delta + I)^{-1} v$. [28]	$\frac{\partial \underline{U}}{\partial t} + (\underline{\overline{U}} \cdot \nabla)\underline{U} + (\nabla\underline{\overline{U}})^T \cdot \underline{U} = -\nabla p + \nu\nabla^2 \underline{U} + \underline{f}$, $\nabla \cdot \underline{\overline{U}} = 0, (I - \alpha^2\nabla^2)\underline{\overline{U}} = \underline{U}$.
(6)	$(\frac{\partial}{\partial t} + u \cdot \nabla)v + v_j \nabla u^j + \nabla P_{tot} = \nu\alpha^2\Delta v + F$, $\nabla \cdot u = 0$, $v = u - \alpha^2\Delta u$, $P_{tot} = P - \frac{1}{2}\lvert u\rvert^2 - \frac{\alpha^2}{2}\lvert\nabla u\rvert^2$. [15]	$\frac{\partial \underline{U}}{\partial t} + (\underline{\overline{U}} \cdot \nabla)\underline{U} + (\nabla\underline{\overline{U}})^T \cdot \underline{U} = -\nabla\overline{p} + \nu\nabla^2 \underline{U} + \underline{f}$, $\nabla \cdot \underline{\overline{U}} = 0$, $(I - \alpha^2\nabla^2)\underline{\overline{U}} = \underline{U}$, $\overline{p} = p - \frac{1}{2}\lvert\underline{\overline{U}}\rvert^2 - \frac{\alpha^2}{2}\lvert\nabla\underline{\overline{U}}\rvert^2$.
	$\partial_t v + u \cdot \nabla v + v_j \nabla u^j$, $+\nabla(p - \frac{1}{2}\lvert u\rvert^2 - \frac{\alpha^2}{2}\lvert\nabla u\rvert^2) = \nu\Delta v$, $\nabla \cdot u = 0$, $v \equiv u - \alpha^2\Delta u$. [16]	
	$\frac{\partial v}{\partial t} + \hat{v} \cdot \nabla v + \nabla\hat{v}^T \cdot v + \nabla p = \nu\nabla^2 v + f$, $\nabla \cdot \hat{v} = 0$, $v = (1 - \alpha^2\nabla^2)\hat{v}$, $p = P - \frac{1}{2}\lvert\hat{v}\rvert^2 - \frac{\alpha^2}{2}\lvert\nabla\hat{v}\rvert^2$. [17]	
(7)	$\frac{\partial}{\partial t} v - \nu\Delta v + (u \cdot \nabla)v + \sum_{j=1}^{3} v_j \nabla u_j + \nabla p = f$, $\nabla \cdot v = 0$, $v = u - \alpha^2\Delta u$. [10]	$\frac{\partial \underline{U}}{\partial t} + (\underline{\overline{U}} \cdot \nabla)\underline{U} + \sum_{j=1}^{3} U_j \nabla\underline{\overline{U}}_j = -\nabla p + \nu\nabla^2 \underline{U} + \underline{f}$, $\nabla \cdot \underline{U} = 0, (I - \alpha^2\nabla^2)\underline{\overline{U}} = \underline{U}$.
(8)	$\frac{\partial}{\partial t} v + (u \cdot \nabla)v + v_j \nabla u_j = \nu\Delta v - \nabla q + f$, $\nabla \cdot u = 0$, $v = u - \frac{\partial}{\partial x_i}(\alpha^2 \delta_{ij} \frac{\partial}{\partial x_j} u)$, $p = q + \frac{1}{2}u^2 - \frac{1}{2}\alpha^2(\frac{\partial}{\partial y}u)^2$. [14]	$\frac{\partial \underline{U}}{\partial t} + (\underline{\overline{U}} \cdot \nabla)\underline{U} + U_j \nabla\underline{\overline{U}}_j = -\nabla\overline{p} + \nu\nabla^2 \underline{U} + \underline{f}$, $\nabla \cdot \underline{\overline{U}} = 0, (I - \alpha^2\nabla^2)\underline{\overline{U}} = \underline{U}$, $\overline{p} = p - \frac{1}{2}\lvert\underline{\overline{U}}\rvert^2 + \frac{\alpha^2}{2}\lvert\nabla\underline{\overline{U}}\rvert^2$.
(9)	$\partial_t u + \overline{u} \cdot \nabla u - (\nabla u)^T \cdot \overline{u} + \nabla p' - \nu\nabla^2 u = \overline{f}$, $\nabla \cdot u = 0$, $p' = p + \overline{u} \cdot u - \frac{1}{2}\overline{u}^2$. [13]	$\frac{\partial \underline{U}}{\partial t} + (\underline{\overline{U}} \cdot \nabla)\underline{U} - (\nabla\underline{U})^T \cdot \underline{\overline{U}} = -\nabla p + \nu\nabla^2 \underline{U} + \underline{f}$, $\nabla \cdot \underline{U} = 0$, $\overline{p} = p + \underline{\overline{U}} \cdot \underline{U} - \frac{1}{2}\lvert\underline{\overline{U}}\rvert^2$.

The incompressible nature of the velocity field $\underline{u}$ does not mean the existence of the divergenceless filtered velocity $\overline{u}$. Only under certain boundary conditions, periodic boundary condition for example, the satisfaction of $\nabla \cdot \underline{u} = 0$ implies the satisfaction of $\nabla \cdot \overline{u} = 0$ [6]. This means that when $\nabla \cdot \overline{u} \neq 0$, the mechanical energy E ($\equiv \frac{1}{2}\int |\underline{u}|^2 d\Omega$) is no longer conserved. It is worthy to note

Table 3
The computed L_2 error norms and the corresponding spatial rates of convergence (R.O.C.) for the classical Navier–Stokes equations calculated at $Re = 1000$ and $t = 3$.

Variable\no. of grids	20^2	40^2	80^2	R.O.C.
u	6.509×10^{-2}	5.817×10^{-4}	6.445×10^{-5}	4.313040
v	6.456×10^{-2}	5.817×10^{-4}	6.445×10^{-5}	4.318457
p	6.169×10^{-2}	8.291×10^{-3}	2.091×10^{-3}	2.424542

Table 4
The computed L_2 error norms and the corresponding spatial rates of convergence (R.O.C.) for the Leray-α equations calculated at $Re = 1000$ and $t = 3$.

Variable\no. of grids	80^2	120^2	160^2	R.O.C.
u	1.043×10^{-3}	3.046×10^{-4}	1.146×10^{-4}	2.828398
v	1.167×10^{-3}	3.413×10^{-4}	1.284×10^{-4}	2.834524
p	3.397×10^{-3}	1.287×10^{-3}	6.477×10^{-4}	2.292221
$\overline{u}$	1.037×10^{-3}	3.037×10^{-4}	1.144×10^{-4}	2.819189
$\overline{v}$	1.162×10^{-3}	3.405×10^{-4}	1.282×10^{-4}	2.826561

Table 5
The computed L_2 error norms and the corresponding spatial (R.O.C.) for the Navier–Stokes-α equations calculated at $Re = 1000$ and $t = 3$.

Variable\no. of grids	40^2	80^2	160^2	R.O.C
u	6.059×10^{-3}	1.060×10^{-3}	1.160×10^{-4}	3.997781
v	6.839×10^{-3}	1.188×10^{-3}	1.301×10^{-4}	3.899497
p	1.585×10^{-2}	3.422×10^{-3}	6.499×10^{-4}	3.623956
$\overline{u}$	5.975×10^{-3}	1.055×10^{-3}	1.157×10^{-4}	3.991342
$\overline{v}$	6.757×10^{-3}	1.182×10^{-3}	1.300×10^{-4}	3.875471

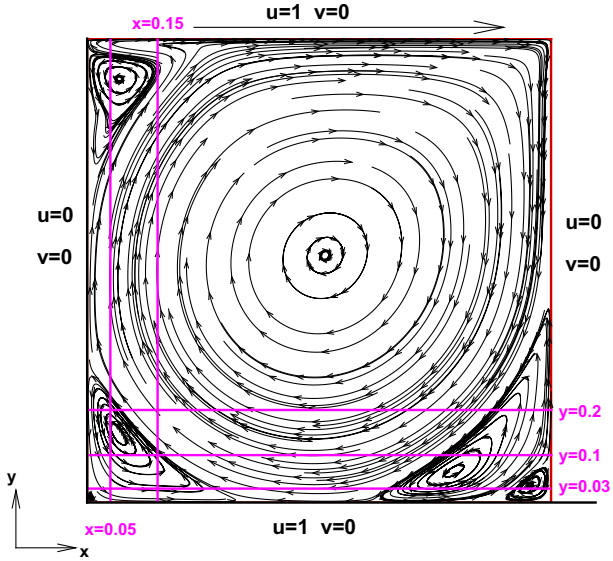

Fig. 1. Illustration of the boundary conditions for the lid-driven cavity flow problem and the lines ($x = 0.05$ and $0.15; y = 0.2, 0.1$ and 0.03) along which the computed solutions are compared.

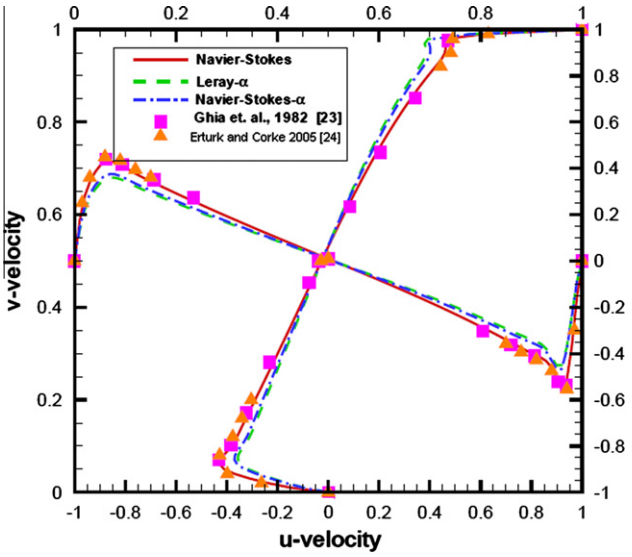

Fig. 2. Comparison of the currently simulated mid-plane velocity profiles $u(x, 0.5)$ and $v(0.5, y)$ with those of Ghia et al. and Erturk and Corke.

that Leray-α model can conserve the energy E in $L^2(\underline{u})$ norm in the sense that $\frac{dE}{dt}$ has association with the energy dissipation rate $\frac{1}{2}\int \underline{\omega}\cdot\underline{\omega} d\Omega$, where $\underline{\omega} \equiv \nabla \times \underline{u}$. While energy is conserved, helicity is not conserved in the Leray-α model equations [6]. For completeness, the Leray-α equations in the literature are tabulated in Table 1.

2.2. NS-α (or LANS-α) model equations

The set of NS equations in (1) and (2) supports the Kelvin theorem. Consequently, a regularization principle possessing the correct circulation properties is desirable to apply. In the Lagrangian averaging context, each fluid loop is advected with the smoothed transport velocity through the regularization by Kelvin filtering [12]. The resulting equations governing the smoothed solenoidal flow field $\nabla \cdot \overline{\underline{u}} = 0$ are as follows [13,14]

$$\underline{u}_t + \overline{\underline{u}} \cdot \nabla \underline{u} + (\nabla \overline{\underline{u}})^T \cdot \underline{u} = -\nabla P + \frac{1}{Re}\nabla^2 \underline{u}, \tag{7}$$

$$\nabla \cdot \overline{\underline{u}} = 0. \tag{8}$$

In the above, P is expressed as [15–17]

$$P = p - \frac{1}{2}|\overline{\underline{u}}|^2 + \frac{\alpha^2}{2}|\nabla \overline{\underline{u}}|^2. \tag{9}$$

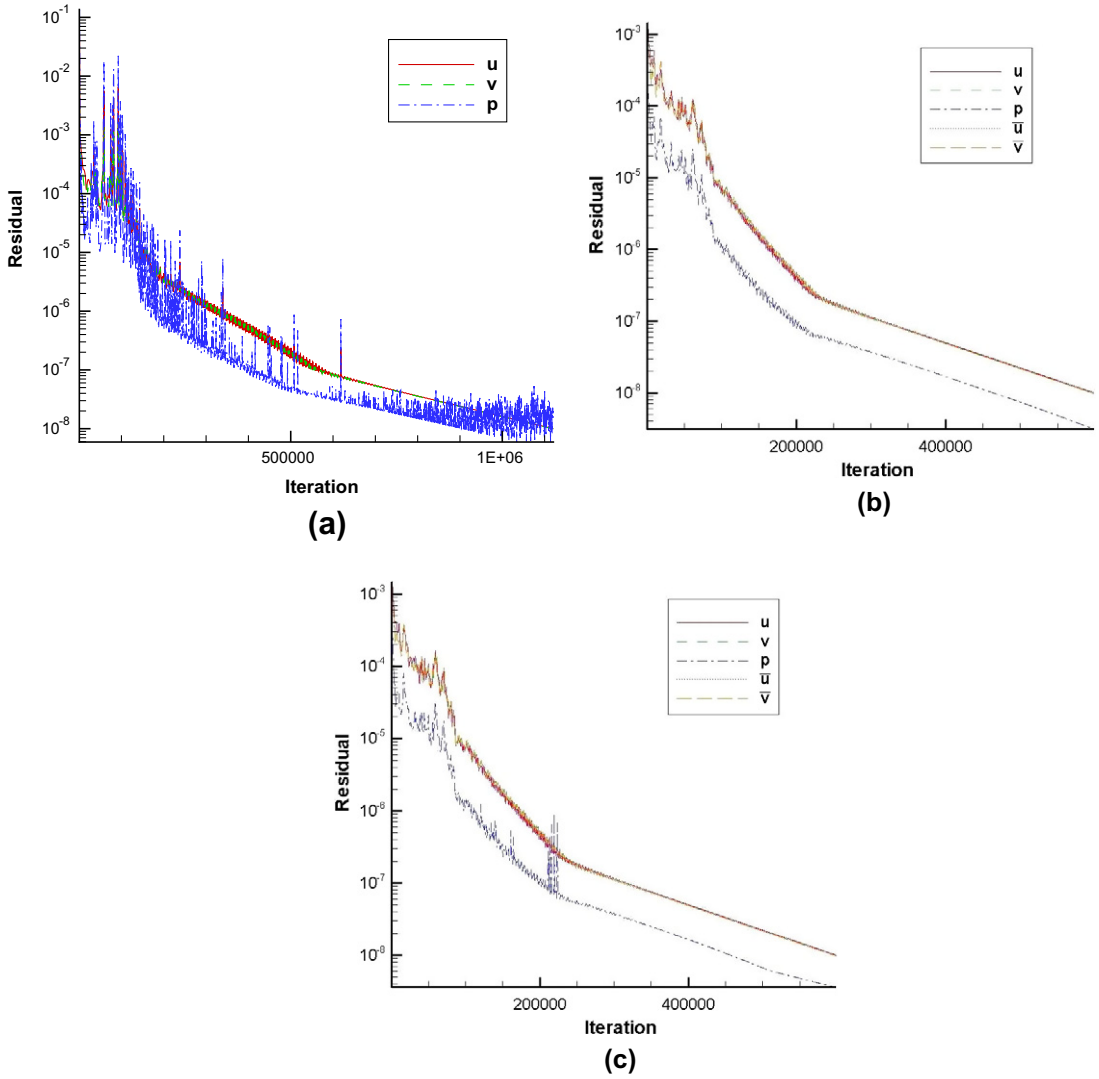

Fig. 3. The residual reduction plots for the lid-driven cavity problem. (a) Navier–Stokes; (b) Leray-α; and (c) Navier–Stokes-α.

For the case with zero viscosity, Eq. (7) turns out to be the *Euler—Poincare'* equation accommodating the action P defined above [18]

$$\underline{u}_t + \overline{\underline{u}} \cdot \nabla \underline{u} + (\nabla \overline{\underline{u}})^T \cdot \underline{u} = -\nabla P. \tag{10}$$

Since Eq. (10) is classified to be *Euler—Poincare'*, the Kelvin–Noether circulation theorem holds true in the sense that $\frac{dI}{dt} = 0$, where $I(t) \equiv \int \overline{\underline{u}} \cdot \alpha^2 \nabla^2 \overline{\underline{u}} d\Omega$ [18]. Note that Eq. (10) is derived directly by applying the smoothing operator $(1 - \alpha^2 \nabla^2)^{-1}$ to the transport velocity in Euler's equation. The above equation is also called as the higher dimensional Camassa–Holm equation which is used often to describe the geodesic motion [12].

As $Re \neq 0$, the elliptic–parabolic set of differential Eqs. (7)–(9) is called as the viscous Camassa–Holm equations [19]. When smoothing the transport velocity $\underline{u}$ through the differential operator $(1 - \alpha^2 \nabla^2)^{-1}$, both of the forward and backward cascades are suppressed for the wave number having an order greater than O $(1/\alpha)$ [18]. Under the circumstances, α, which corresponds to the length scale, shown in the smoothing operator becomes essential. This smoothing of the velocity vector makes, however, the dynamics of the Euler flow essentially unchanged at smaller wave numbers.

In comparison with the Leray-α equations, two additional terms in the LANS-α model guarantee the regularized flow to be consistent with the Kelvin's circulation theorem [9]. One can also recast Eqs. (8)–(10) to their equivalent equations in LES template. The turbulent stress tensor is the sum of the Leray-α stress tensor and the additional turbulent stress term, which is $-\alpha^2 H^{-1}(\partial_i \overline{u}_k \partial_j \overline{u}_k)$, that plays the role to preserve the Kelvin's circulation [9].

When employing the regularization strategy to model a subgrid scale flow it is desired to preserve some physical constraints, such as the energy conservation and the helicity conservation, on the Navier–Stokes equations. Satisfaction of the Kelvin's circulation theorem and the symmetry preservation is also essential to successfully model a subgrid scale flow motion. For this reason, more complex NS-α models were developed. In NS-α model, it conserves energy $E_\alpha = \frac{1}{2} \int \underline{u} \cdot \overline{\underline{u}} d\Omega$ in the $H^1_\alpha(\overline{\underline{u}})$ norm [6]. The change of E_α has close association with the NS-α energy dissipation rate $\Omega_\alpha = \frac{1}{2} \int \underline{\omega} \cdot \overline{\underline{\omega}} d\Omega$. In the regularization models summarized in Table 2, a different representation of P given below can be seen in [14]

$$P = p - \frac{1}{2}|\overline{\underline{u}}|^2 + \frac{\alpha^2}{2}|\nabla \overline{\underline{u}}|^2. \tag{11}$$

3. Numerical method

3.1. Compact scheme for the spatial derivative terms

To describe the numerical scheme for approximating the spatial derivative terms, the transport equation given below for ϕ is considered at a constant diffusion coefficient k

$$a\frac{\partial \phi}{\partial x} + b\frac{\partial \phi}{\partial y} - k\left(\frac{\partial^2 \phi}{\partial x^2} + \frac{\partial^2 \phi}{\partial y^2}\right) = f. \tag{12}$$

In the above, two coefficients a and b are denoted as the constant velocities along the respective x- and y-direction, and f is a source term. The first-order and second-order spatial derivative terms

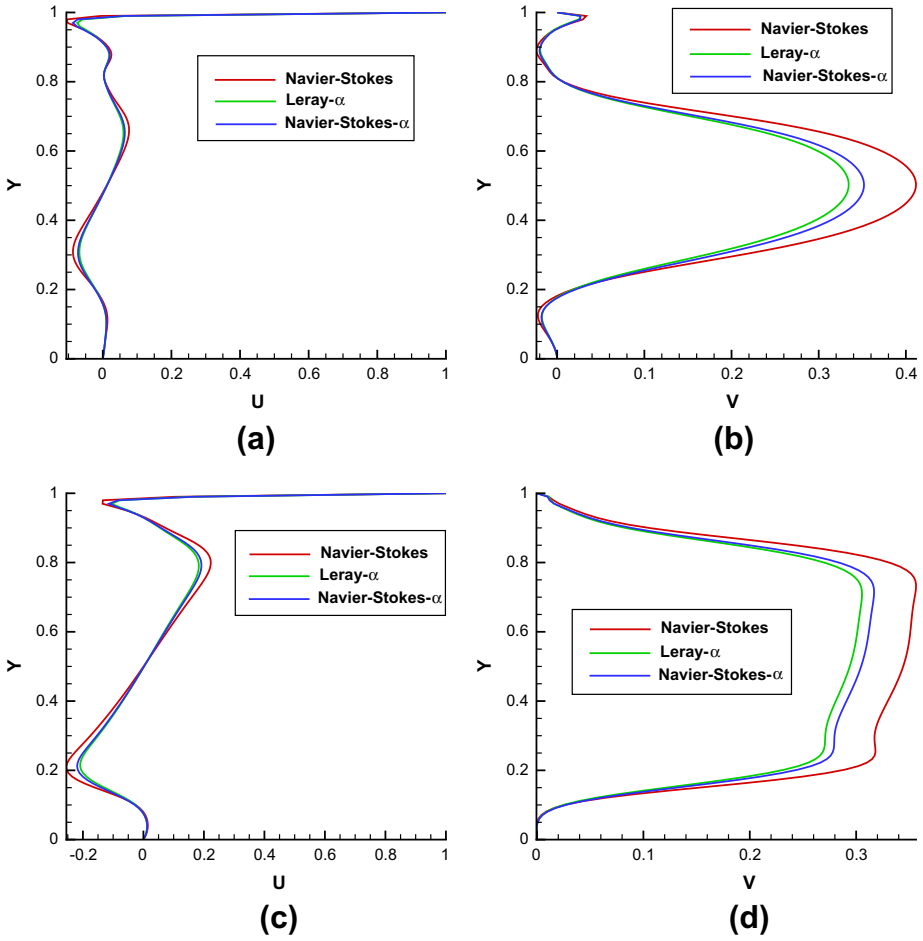

Fig. 4. Comparison of the predicted velocity profiles at different cutting planes for the lid-driven cavity problem. (a) and (b) $x = 0.05$ and (c) and (d) $x = 0.15$.

shown in Eq. (12) will be both approximated in a domain with the uniform grid size $\Delta x = \Delta y = h$.

The first-order derivative term $\frac{\partial \phi}{\partial x}$ and the second-order derivative term $\frac{\partial^2 \phi}{\partial x^2}$ in Eq. (12) are approximated in a coupled fashion. In the combined compact finite difference context, the adopted strategy falls into the following three-point framework

$$a_1 \frac{\partial \phi}{\partial x}|_{i-1} + \frac{\partial \phi}{\partial x}|_i = \frac{1}{h}(c_1\phi_{i-1} + c_2\phi_i + c_3\phi_{i+1}) - h\left(b_1 \frac{\partial^2 \phi}{\partial x^2}|_{i-1} + b_2 \frac{\partial^2 \phi}{\partial x^2}|_i + b_3 \frac{\partial^2 \phi}{\partial x^2}|_{i+1}\right), \quad (13)$$

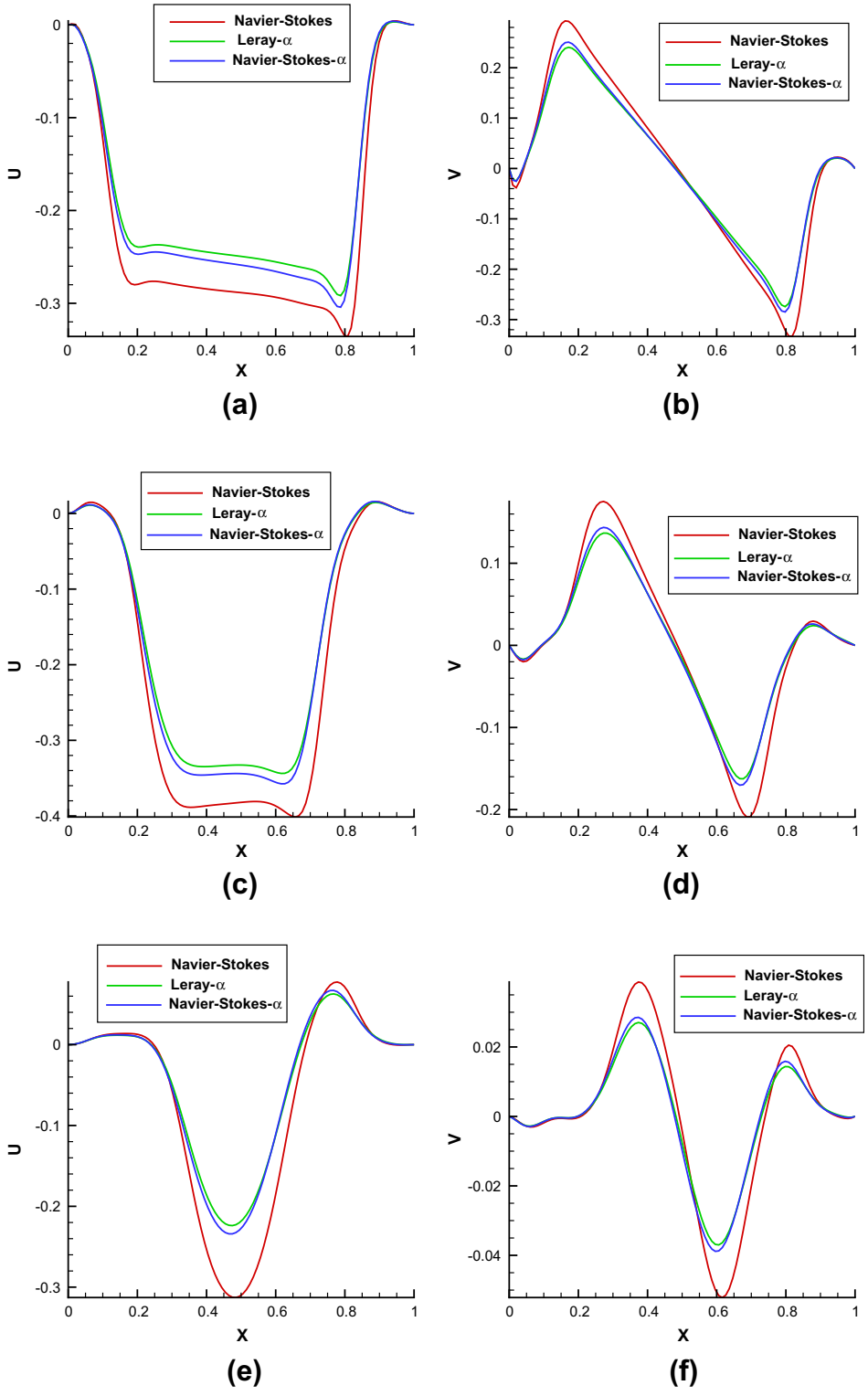

Fig. 5. Comparison of the predicted velocity profiles at different cutting planes for the lid-driven cavity problem. (a) and (b) $y = 0.2$; (c) and (d) $y = 0.1$; (e) and (f) $y = 0.03$.

$$\bar{b}_1\frac{\partial^2\phi}{\partial x^2}|_{i-1}+\frac{\partial^2\phi}{\partial x^2}|_i+\bar{b}_3\frac{\partial^2\phi}{\partial x^2}|_{i+1}=\frac{1}{h^2}(\bar{c}_1\phi_{i-1}+\bar{c}_2\phi_i+\bar{c}_3\phi_{i+1})-\frac{1}{h}\left(\bar{a}_1\frac{\partial\phi}{\partial x}|_{i-1}+\bar{a}_2\frac{\partial\phi}{\partial x}|_i+\bar{a}_3\frac{\partial\phi}{\partial x}|_{i+1}\right). \quad (14)$$

The other two terms $\frac{\partial\phi}{\partial y}$ and $\frac{\partial^2\phi}{\partial y^2}$ can be similarly expressed along the y-direction. Note that the compact representations of the terms $\frac{\partial\phi}{\partial x}|_i$ and $\frac{\partial^2\phi}{\partial x^2}|_i$ are not independent of each other. They will be rather coupled through the terms $\frac{\partial\phi}{\partial x}|_{i-1}, \frac{\partial\phi}{\partial x}|_i, \frac{\partial\phi}{\partial x}|_{i+1}, \frac{\partial^2\phi}{\partial x^2}|_{i-1}, \frac{\partial^2\phi}{\partial x^2}|_i, \frac{\partial^2\phi}{\partial x^2}|_{i+1}, \phi_{i-1}, \phi_i$ and ϕ_{i+1}. For ease of description of the numerical method, only the case involving a positive convective coefficient is dealt with. For the negative convective coefficient case, its derivation will be the same.

3.1.1. Compact scheme for the second-order derivative term

The second-order derivative terms are normally approximated by the central schemes. As a result, the weighting coefficients shown in Eq. (14) can be determined solely by the modified equation analysis for getting a better spatial accuracy. Derivation of the coefficients $\bar{a}_1, \bar{a}_2, \bar{a}_3, \bar{b}_1, \bar{b}_3, \bar{c}_1, \bar{c}_2$, and $\bar{c}_3$ in (13) and (14) is as follows. We start by applying the Taylor series expansions for $\phi_{i\pm1}, \frac{\partial\phi}{\partial x}|_{i\pm1}$ and $\frac{\partial^2\phi}{\partial x^2}|_{i\pm1}$ with respect to $\phi_i, \frac{\partial\phi}{\partial x}|_i$ and $\frac{\partial^2\phi}{\partial x^2}|_i$ and, then, eliminate the leading error terms derived in the modified equations. Elimination of leading error terms of different differential orders shown in the modified equation enables us to get eight algebraic equations for Eq. (14). By solving these algebraic equations, the coefficients in Eq. (14) can be derived as $\bar{a}_1=-\frac{9}{8}, \bar{a}_2=0, \bar{a}_3=\frac{9}{8}, \bar{b}_1=-\frac{1}{8}, \bar{b}_3=-\frac{1}{8}, \bar{c}_1=3, \bar{c}_2=-6, \bar{c}_3=3$. The resulting derived modified equation for $\frac{\partial^2\phi}{\partial x^2}$ is $\frac{\partial^2\phi}{\partial x^2}=\frac{\partial^2\phi}{\partial x^2}|_{exact}+\frac{h^6}{20{,}160}\frac{\partial^8\phi}{\partial x^8}+\frac{h^8}{604{,}800}\frac{\partial^{10}\phi}{\partial x^{10}}+O(h^{12})+\cdots$ using the presently derived set of coefficients. This implies that the proposed scheme for $\frac{\partial^2\phi}{\partial x^2}$ has the spatial accuracy order of sixth.

3.1.2. Wavenumber optimized compact scheme for the first-order derivative term

The coefficients a_1, b_1-b_3, c_1-c_3 in Eq. (13) are partly determined by applying the Taylor series expansions on the terms $\phi_{i\pm1}, \frac{\partial\phi}{\partial x}|_{i-1}$ and $\frac{\partial^2\phi}{\partial x^2}|_{i\pm1}$ with respect to $\phi_i, \frac{\partial\phi}{\partial x}|_i$ and $\frac{\partial^2\phi}{\partial x^2}|_i$. By eliminating the leading six error terms derived in the modified equation, a set of algebraic equations for Eq. (13) can be derived. One algebraic equation is needed to uniquely determine all the seven introduced coefficients shown in Eq. (13).

For an accurate prediction of the first-order derivative term from Eq. (13), it is desired to retain the dispersive nature embedded in $\frac{\partial\phi}{\partial x}$ since dispersion relation serves as a bridge between the angular frequency and the wavenumber of the first-order

Table 6
Comparison of the computed divergence errors for the lid-driven cavity problem using the two investigated models.

Models	$\nabla\cdot\underline{u}$	$\nabla\cdot\underline{\bar{u}}$
Navier–Stokes	6.918×10^{-6}	
Leray-α	3.549×10^{-6}	2.888839
Navier–Stokes-α	3.344468×10^{-6}	0.495072

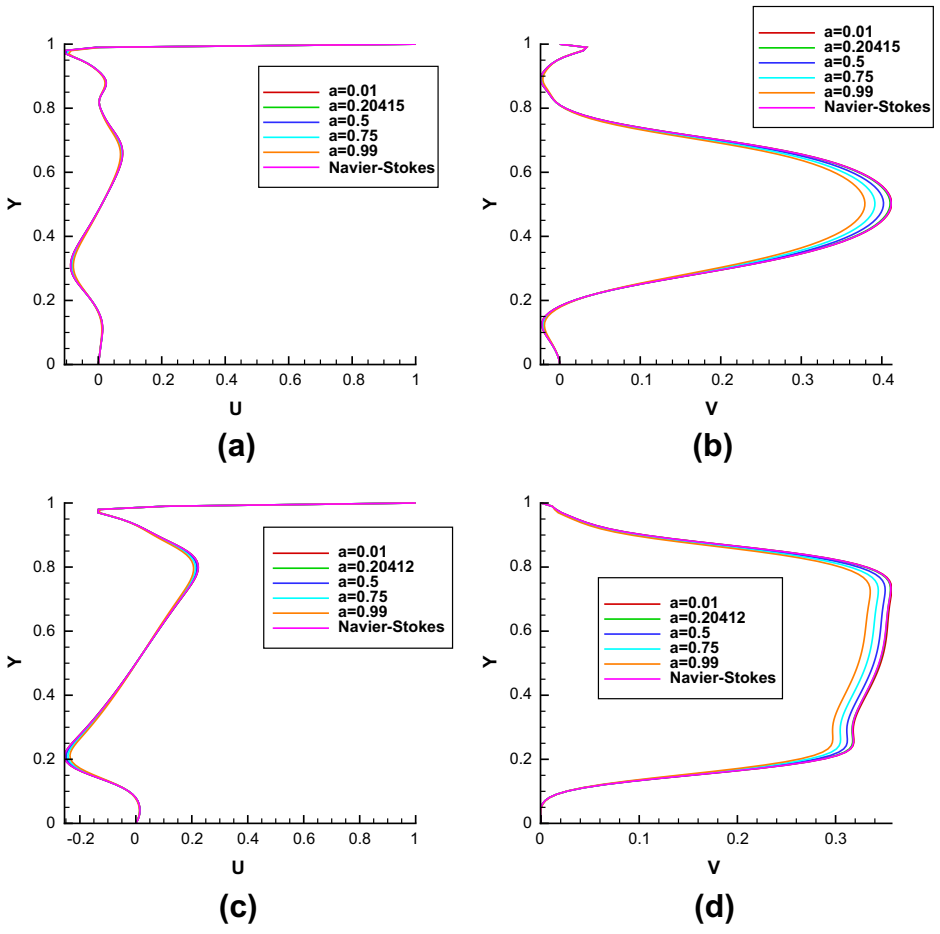

Fig. 6. Comparison of the predicted velocity profiles for the Leray-α model at different values of α for the lid-driven cavity problem. (a) and (b) $x=0.05$; (c) and (d) $x=0.15$.

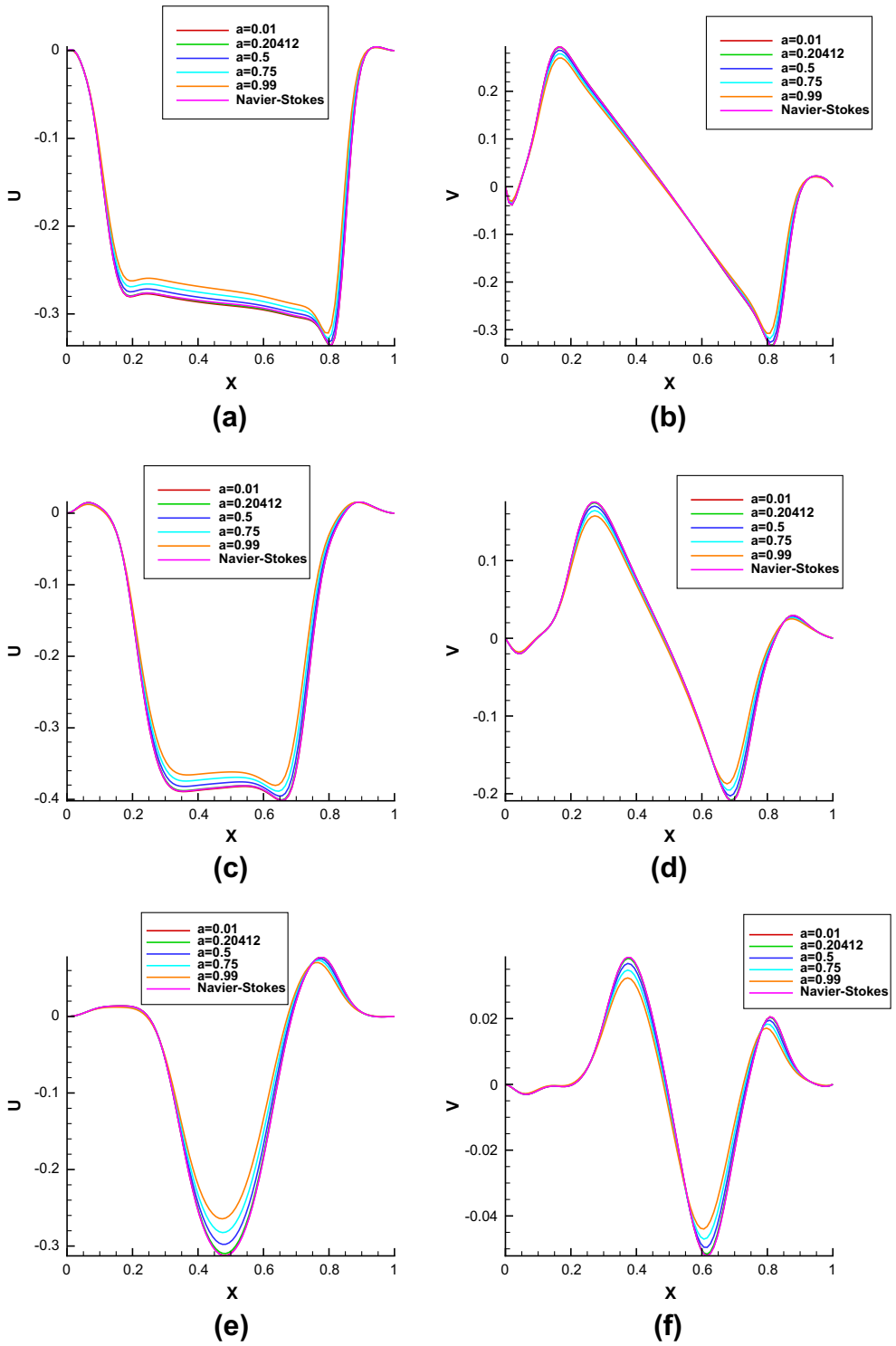

Fig. 7. Comparison of the predicted velocity profiles for the Leray-α model at different values of α for the lid-driven cavity problem. (a) and (b) $y = 0.2$; (c) and (d) $y = 0.1$ (e) and (f) $y = 0.03$.

dispersive term [20]. In other words, the solution can be accurately predicted provided that the exact dispersion relation is well preserved. To preserve dispersion relation, Fourier transform and its inverse for ϕ given below are applied

$$\tilde{\phi}(\alpha) = \frac{1}{2\pi} \int_{-\infty}^{+\infty} \phi(x)\ \exp(-\mathbf{i}\alpha x)\ dx, \tag{15}$$

$$\phi(x) = \int_{-\infty}^{+\infty} \tilde{\phi}(\alpha)\ \exp(\mathbf{i}\alpha x)\ d\alpha. \tag{16}$$

The notation $\mathbf{i}$ shown above denotes $\sqrt{-1}$. By performing the Fourier transform on each term shown in Eqs. (13) and (14), the expressions of the actual wavenumber α for these two equations can be derived from

$$\begin{aligned}\mathbf{i}\alpha h(a_1 \exp(-\mathbf{i}\alpha h) + 1) \simeq\ & c_1 \exp(-\mathbf{i}\alpha h) + c_2 + c_3 \exp(\mathbf{i}\alpha h) \\ & - (\mathbf{i}\alpha h)^2 (b_1 \exp(-\mathbf{i}\alpha h) + b_2 + b_3 \\ & \times \exp(\mathbf{i}\alpha h)),\end{aligned} \tag{17}$$

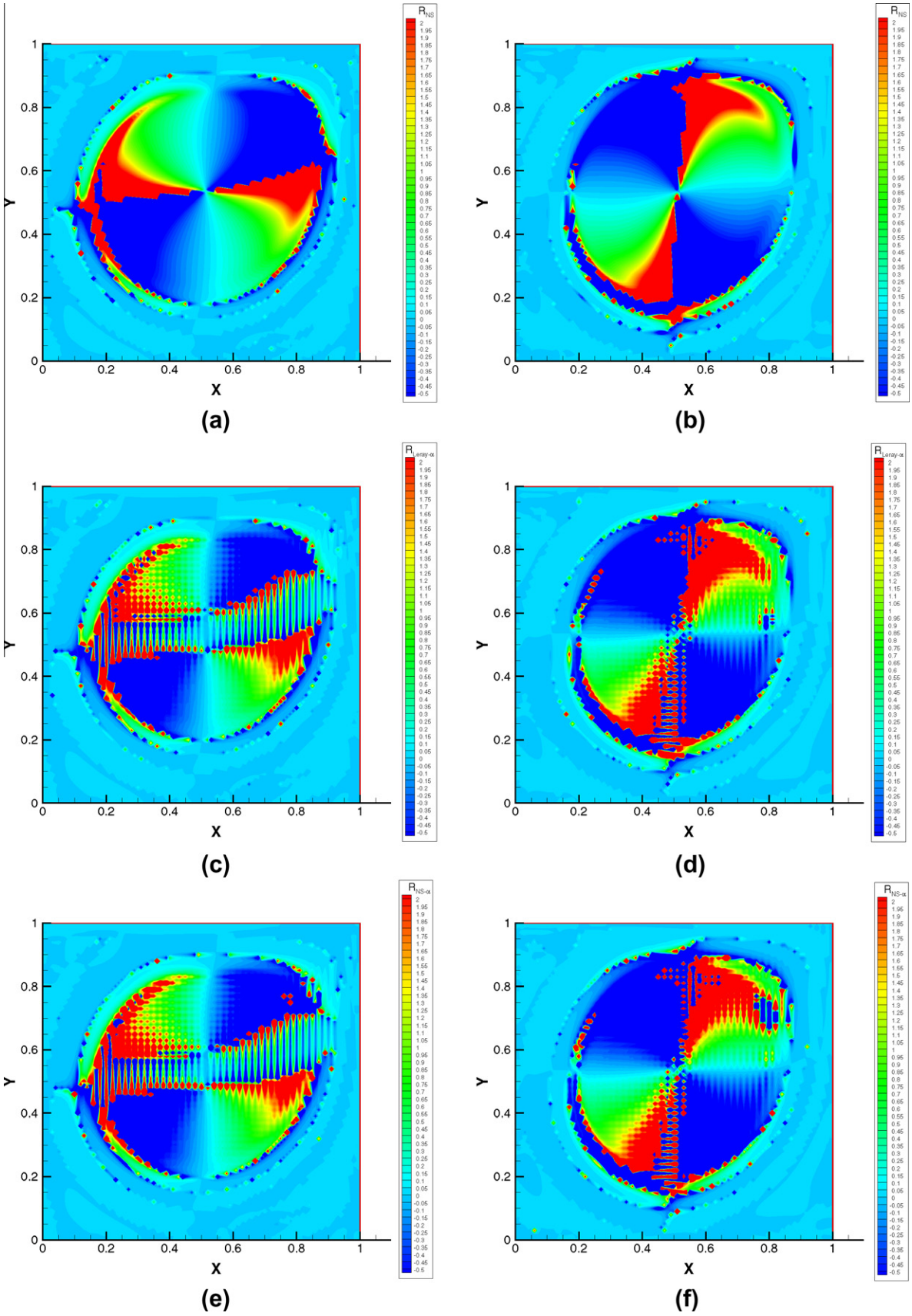

Fig. 8. The computed contours for the lid-driven cavity problem. (a) R_{NS} for u; (b) R_{NS} for v; (c) $R_{Leray\text{-}\alpha}$ for u; (d) $R_{Leray\text{-}\alpha}$ for v; (e) $R_{NS\text{-}\alpha}$ for u; and (f) $R_{NS\text{-}\alpha}$ for v.

$$(\mathbf{i}\alpha h)^2(-\frac{1}{8}\exp(-\mathbf{i}\alpha h)+1-\frac{1}{8}\exp(\mathbf{i}\alpha h)) \simeq 3(\exp(-\mathbf{i}\alpha h)-2+\exp(\mathbf{i}\alpha h))-\frac{8}{9}\mathbf{i}\alpha h(-\exp(-\mathbf{i}\alpha h)+\exp(\mathbf{i}\alpha h)). \quad (18)$$

We are aimed to derive the effective wavenumbers α' and α'' having the same expressions as those shown on the right-hand sides of Eqs. (17) and (18) [20]. Therefore, it is rational for us to express α' and α'' as follows

$$\mathbf{i}\alpha' h(a_1\exp(-\mathbf{i}\alpha h)+1) = c_1\exp(-\mathbf{i}\alpha h)+c_2+c_3\exp(\mathbf{i}\alpha h) - (\mathbf{i}\alpha'' h)^2(b_1\exp(-\mathbf{i}\alpha h)+b_2+b_3\times\exp(\mathbf{i}\alpha h)), \quad (19)$$

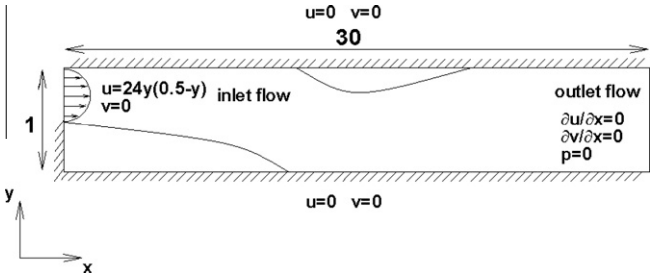

Fig. 9. Illustration of the boundary conditions for the backward-facing step problem.

$$\frac{8}{9}\mathbf{i}\alpha' h(-\exp(-\mathbf{i}\alpha h)+\exp(\mathbf{i}\alpha h)) = 3\exp(-\mathbf{i}\alpha h)-6+3\exp(\mathbf{i}\alpha h)-(\mathbf{i}\alpha'' h)^2(-\frac{1}{8}\exp(-\mathbf{i}\alpha h)+1-\frac{1}{8}\exp(\mathbf{i}\alpha h)). \quad (20)$$

The following expressions for α' and α'' can be derived from Eqs. (19) and (20)

$$\begin{aligned}\alpha' h = {} & -\mathbf{i}(24b_1\exp(-2\mathbf{i}\alpha h)+c_1\exp(-2\mathbf{i}\alpha h)+c_3+c1+24b_1 \\ & +c_2\exp(-\mathbf{i}\alpha h)+24b_2\exp(-\mathbf{i}\alpha h)+24b_3-48b_1 \\ & \times\exp(-\mathbf{i}\alpha h)-8c_1\exp(-\mathbf{i}\alpha h)-48b_3\exp(\mathbf{i}\alpha h)+24b_2 \\ & \times\exp(\mathbf{i}\alpha h)+24b_3\exp(2\mathbf{i}\alpha h)-48b_2+c_2\exp(\mathbf{i}\alpha h) \\ & +c_3\exp(2\mathbf{i}\alpha h)-8c_3\exp(\mathbf{i}\alpha h)-8c_2)/(-8+\exp(\mathbf{i}\alpha h) \\ & -8a_1\exp(-\mathbf{i}\alpha h)+a_1\exp(-2\mathbf{i}\alpha h)-9b_1\exp(-2\mathbf{i}\alpha h) \\ & -9b_2\exp(-\mathbf{i}\alpha h)+9b_2\exp(\mathbf{i}\alpha h)+9b_3\exp(2\mathbf{i}\alpha h)+a_1 \\ & +9b_1-9b_3+\exp(\mathbf{i}\alpha h)), \end{aligned} \quad (21)$$

$$\alpha'' h = \sqrt{-\frac{3\exp(-\mathbf{i}\alpha h)-6+3\exp(\mathbf{i}\alpha h)-\mathbf{i}\alpha' h(-\frac{8}{9}\exp(-\mathbf{i}\alpha h)+\frac{8}{9}\exp(\mathbf{i}\alpha h))}{-\frac{1}{8}\exp(-\mathbf{i}\alpha h)+1-\frac{1}{8}\exp(\mathbf{i}\alpha h)}}. \quad (22)$$

For getting a better dispersive accuracy for α', we set $\alpha h \approx \Re[\alpha' h]$, where $\Re[\alpha' h]$ denotes the real part of $\alpha' h$. This implies that $E(\alpha)$ defined below should be the one having a very small positive magnitude

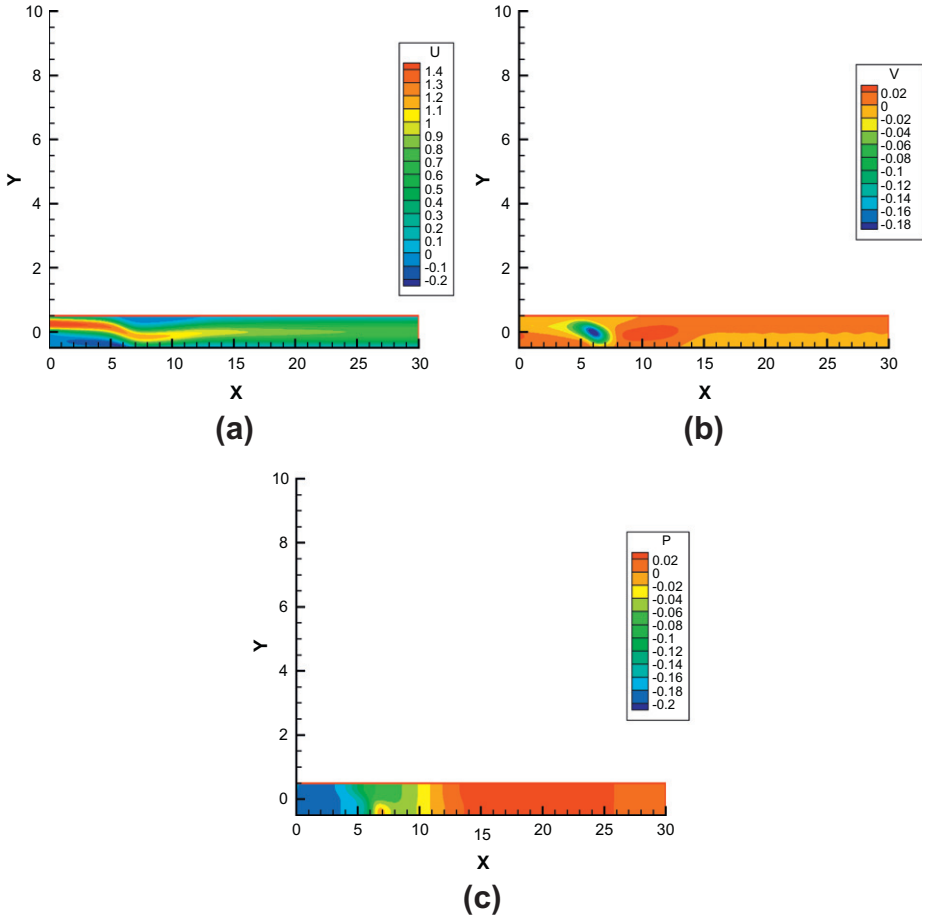

Fig. 10. The contours computed from the Navier–Stokes equations for the backward-facing step problem. (a) u; (b) v; and (c) p.

$$E(\alpha) = \int_{-\frac{\pi}{2}}^{\frac{\pi}{2}} [W(\alpha h - \Re[\alpha' h])]^2 d(\alpha h) = \int_{-\frac{\pi}{2}}^{\frac{\pi}{2}} [W(\gamma - \Re[\gamma'])]^2 d\gamma, \quad (23)$$

where $\gamma = \alpha h$ and $\gamma' = \alpha' h$. Note that Eq. (23) can be integrated analytically provided that the weighting function W shown above is chosen as follows for $A = 72(b_1 + b_3 - a_1 b_2) - 81(b_1^2 + b_2^2 + b_3^2) - 16(1 + a_1^2) + 162 b_1 b_3$, $B = 8(1 + a_1^2) + 18(a_1 b_2 - b_1 + b_3) - 162(b_1 b_2 + b_2 b_3) - 144 a_1 b_3 - 32 a_1)$, $C = 72(a_1 b_2 + b_3 - b_1) + 81(b_1^2 + b_2^2 + b_3^2) - (a_1^2 + 1) + 16 a_1 - 486 b_1 b_3 + 36 a_1 b_3$, $D = 18(b_1 - a_1 b_2 - b_3) + 162(b_1 b_2 + b_2 b_3) - 2 a_1 + 144 a_1 b_3$, and $E = 324 b_1 b_3 - 36 a_1 b_3$

$$W = A + B\cos(\gamma) + C\cos(\gamma)^2 + D\cos(\gamma)^3 + E\cos(\gamma)^4. \quad (24)$$

To get the minimal value of E defined in Eq. (23), the extreme condition $\frac{\partial E}{\partial c_3} = 0$ is applied. The equation enforced to preserve numerical wavenumber will be used together with the other six previously derived algebraic equations by way of the modified

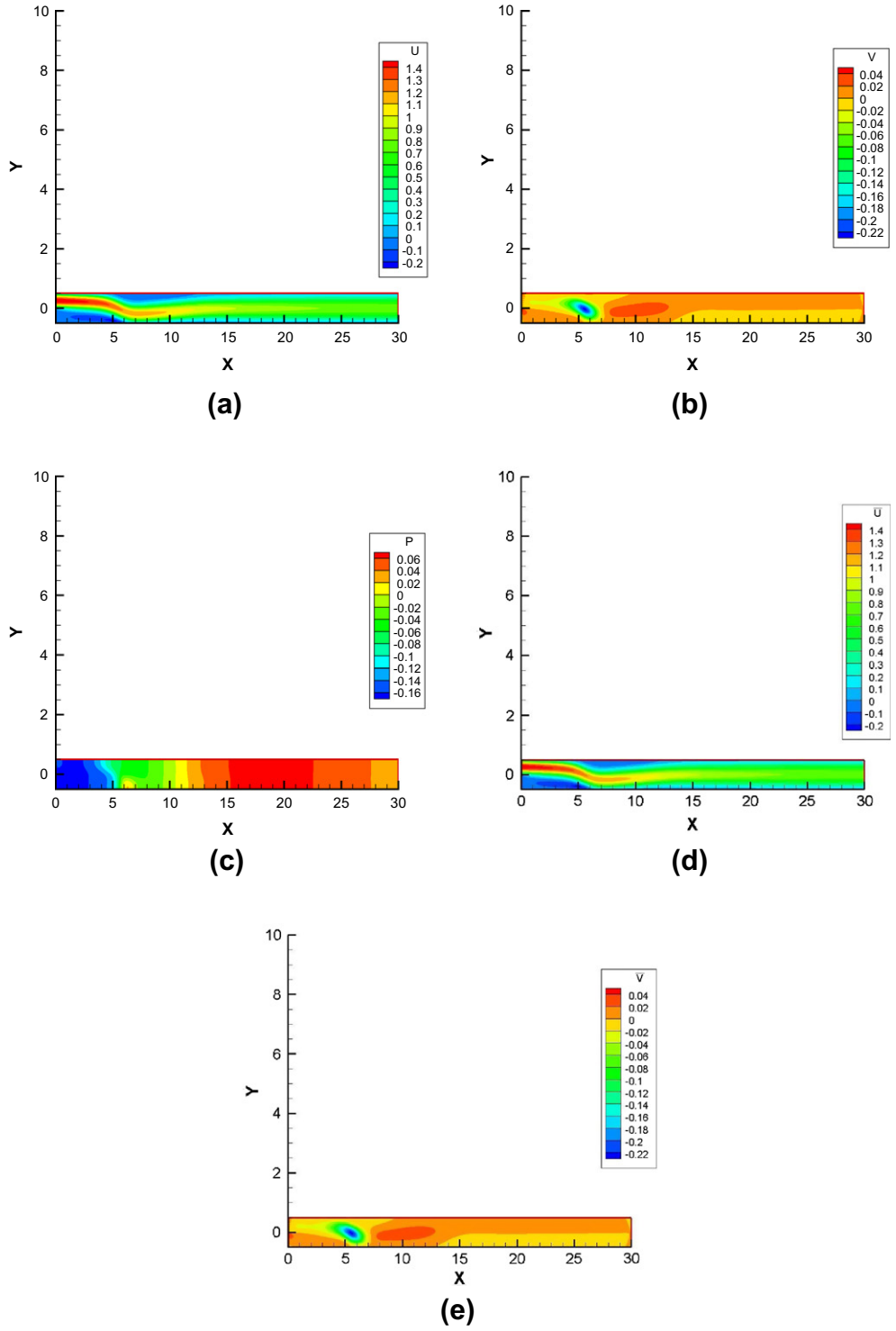

Fig. 11. The contours computed from the Leray-α equations for the backward-facing step problem. (a) u; (b) v; (c) p; (d) $\overline{u}$; and (e) $\overline{v}$.

equation analysis to get the higher dissipation and dispersion accuracies. The resulting seven introduced unknowns can then be uniquely determined as $(a_1, b_1, b_2, b_3, c_1, c_2, c_3) = (0.875, 0.1251282, -0.2487176, 0.0001282, -1.9359611, 1.9969223, -0.0609611)$. We remark here that the wavenumber optimized upwinding scheme developed for $\frac{\partial\phi}{\partial x}$ has the spatial accuracy order of fifth according to the derived modified equation $\frac{\partial\phi}{\partial x} = \frac{\partial\phi}{\partial x}|_{exact} - 0.0007008h^5\frac{\partial^6\phi}{\partial x^6} + 0.0001984h^6\frac{\partial^7\phi}{\partial x^7} - 0.0000498h^7\frac{\partial^8\phi}{\partial x^8} + O(h^8) + \cdots$.

3.2. Incompressible flow solver

Calculation of the regularized flow equations begins with solving the following two equations in the projection step

$$\frac{\underline{u}^{n+1} - \underline{u}^{n+\frac{1}{2}}}{\Delta t} = -\nabla p^{n+1}, \tag{25}$$

$$\nabla \cdot \underline{u}^{n+1} = 0. \tag{26}$$

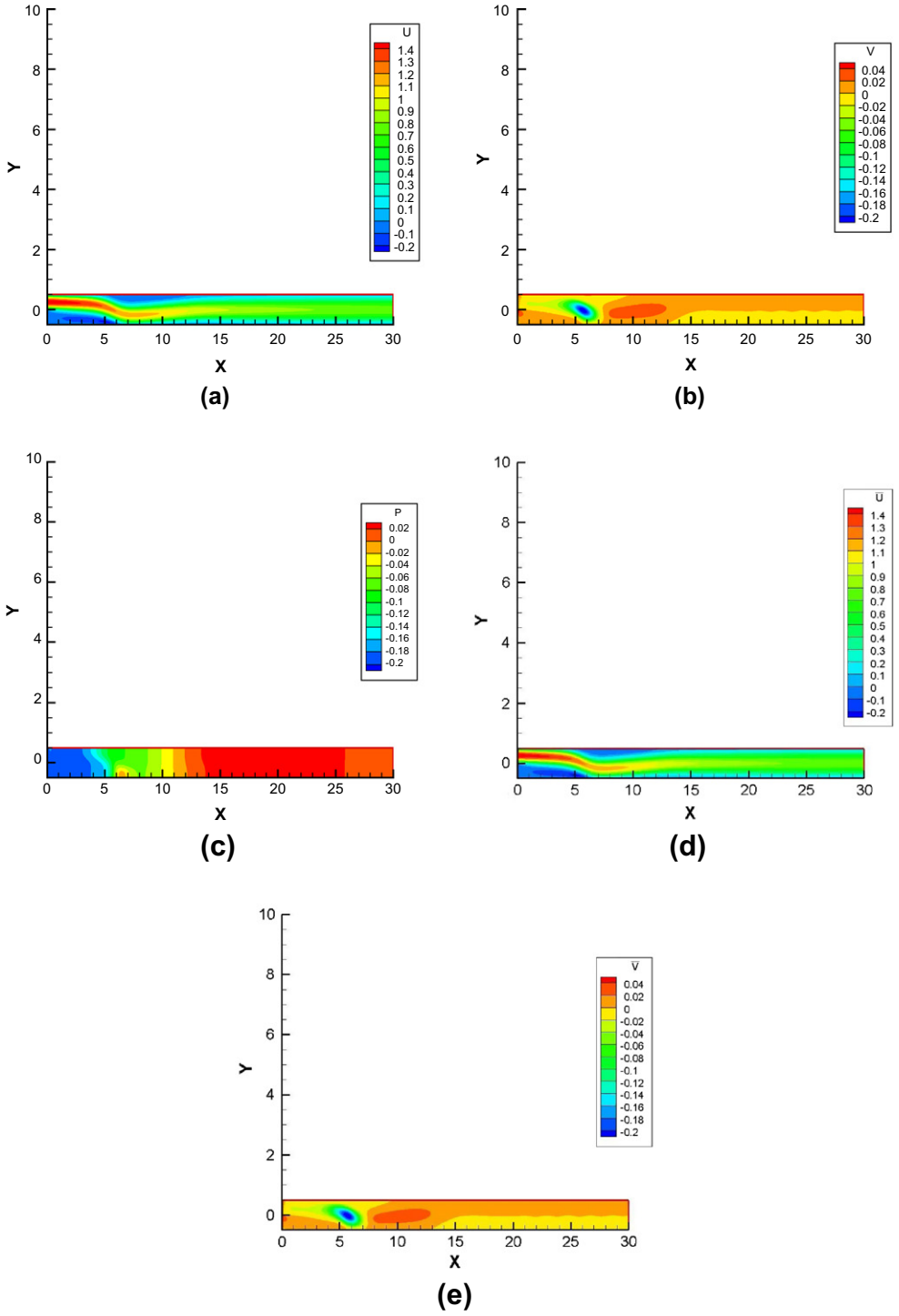

Fig. 12. The contours computed from the Navier–Stokes-α equations for the backward-facing step problem. (a) u; (b) v; (c) p; (d) $\overline{u}$; and (e) $\overline{v}$.

Substitution of Eq. (25) into the semi-discretized momentum equation leads to

$$\frac{\underline{u}^{n+1}-\underline{u}^{n}}{\Delta t}+(\underline{u}^{n+\frac{1}{2}}\cdot\nabla)\underline{u}^{n+\frac{1}{2}}-\frac{1}{Re}\nabla^2\underline{u}^{n+\frac{1}{2}}+\nabla p^{n+1}=M_1+M_2, \tag{27}$$

where $M_1=[(\underline{u}^{n+\frac{1}{2}}\cdot\nabla)\nabla p^{n+1}+(\nabla p^{n+1}\cdot\nabla)\underline{u}^{n+\frac{1}{2}}-\frac{1}{Re}\nabla^2(\nabla p^{n+1})]\Delta t$ and $M_2=-[(\nabla p^{n+1}\cdot\nabla)\nabla p^{n+1}]\Delta t^2$. Let $p^{n+1}=p^*+p'$, the pressure-gradient step is decomposed into the step given by $\frac{\underline{u}^*-\underline{u}^{n+\frac{1}{2}}}{\Delta t}=-\nabla p^*$ and the step given by $\frac{\underline{u}^{n+1}-\underline{u}^*}{\Delta t}=-\nabla p'$, where p^* is an intermediate pressure. Then, Eq. (27) is reformulated as

$$\frac{\underline{u}^{n+1}-\underline{u}^{n}}{\Delta t}+(\underline{u}^*\cdot\nabla)\underline{u}^*-\frac{1}{Re}\nabla^2\underline{u}^*+\nabla p^*=-\nabla p'+M_3+M_4, \tag{28}$$

where $M_3=[(\underline{u}^*\cdot\nabla)\nabla p'+(\nabla p'\cdot\nabla)\underline{u}^*]\Delta t-\frac{1}{Re}\nabla(\nabla\cdot\underline{u}^*)$ and $M_4=-[(\nabla p'\cdot\nabla)\nabla p']\Delta t^2$. In order to reduce the computational cost, the following algorithm is employed [21]

Given the solutions of the velocity $\underline{u}_1^*$, pressure p_0^* and p_0'.

For $s=1,2,\ldots$

$$\frac{\underline{u}_s^{n+1}-\underline{u}^{n}}{\Delta t}+\underline{u}_s^*\cdot\nabla\underline{u}_s^*-\frac{1}{Re}\nabla^2\underline{u}_s^*+\nabla p_{s-1}^*=-\nabla p_{s-1}', \tag{29}$$

$$p_s^*=p_{s-1}^*+p_s', \tag{30}$$

$$\underline{u}_{s+1}^*=\underline{u}_s^{n+1}-\Delta t\nabla p_s'. \tag{31}$$

By performing the divergence operator on $\frac{\underline{u}^{n+1}-\underline{u}^*}{\Delta t}=-\nabla p'$, we can get $\nabla\cdot\underline{u}^{n+1}=\nabla\cdot\underline{u}^*-\Delta t\nabla^2p'$. Enforcement of $\nabla\cdot\underline{u}^{n+1}=0$ yields $\nabla^2p'=\frac{\nabla\cdot\underline{u}^*}{\Delta t}$. At each interior point (i,j), the central approximation given below for $\nabla^2p'=\frac{\nabla\cdot\underline{u}^*}{\Delta t}$ yields

$$2(\frac{1}{\Delta x^2}+\frac{1}{\Delta y^2})p_{i,j}'=-\frac{\nabla\cdot\underline{u}_{i,j}^*}{\Delta t}+\frac{1}{\Delta x^2}(p_{i-1,j}'+p_{i+1,j}')+\frac{1}{\Delta y^2}(p_{i,j-1}'+p_{i,j+1}'). \tag{32}$$

By omitting $\frac{1}{\Delta x^2}(p_{i-1,j}'+p_{i+1,j}')+\frac{1}{\Delta y^2}(p_{i,j-1}'+p_{i,j+1}')$, the following equation is derived

$$p_{i,j}'=-\frac{\Delta x^2\Delta y^2}{2(\Delta x^2+\Delta y^2)\Delta t}\nabla\cdot\underline{u}_{i,j}^*. \tag{33}$$

The above formulation for p' may over-estimate the predicted pressure due to the omitted term. For the compensation of this omission, Eq. (33) is used first to get the following pressure correction them p'^*

$$p_{i,j}'^*=-\frac{\Delta x^2\Delta y^2}{2(\Delta x^2+\Delta y^2)\Delta t}\nabla\cdot\underline{u}_{i,j}^*. \tag{34}$$

This is followed by calculating the pressure correction term p' from p'^* according to

$$p_{i,j}'=p_{i,j}'^*+\frac{\Delta y^2}{2(\Delta x^2+\Delta y^2)}(p_{i-1,j}'^*+p_{i+1,j}'^*)+\frac{\Delta x^2}{2(\Delta x^2+\Delta y^2)}(p_{i,j-1}'^*+p_{i,j+1}'^*). \tag{35}$$

3.3. Three-point sixth-order Helmholtz scheme

To get a more accurate Helmholtz solution, the following prototype equation is considered

$$\frac{\partial^2u}{\partial x^2}-ku=f(x). \tag{36}$$

Denoting the values of $\partial^2u/\partial x^2, \partial^4u/\partial x^4$ and $\partial^6u/\partial x^6$ at the nodal point i as $\frac{\partial^2u}{\partial x^2}|_i=s_i, \frac{\partial^4u}{\partial x^4}|_i=v_i, \frac{\partial^6u}{\partial x^6}|_i=w_i$, the compact scheme for (36) will be developed below at the point i [22]. Derivation of the scheme starts with relating the terms v, s and w with u as follows

$$\delta_0h^6w_i+\gamma_0h^4v_i+\beta_0h^2s_i=\alpha_1u_{i+1}+\alpha_0u_i+\alpha_{-1}u_{i-1}. \tag{37}$$

It is legitimate to set $\alpha_1=\alpha_{-1}$ since Eq. (36) is elliptic in nature. Derivation of the Helmholtz scheme is followed by expanding the terms $u_{i\pm1}$ with respect to u_i. Substitution of these Taylor-series expansion equations into Eq. (37) leads to

$$\begin{aligned}\delta_0h^6w_i+\gamma_0h^4v_i+\beta_0h^2s_i=(\alpha_0+2\alpha_1)u_i&+\frac{h^2}{2!}(2\alpha_1)\frac{\partial^2u_i}{\partial x^2}\\&+\frac{h^4}{4!}(2\alpha_1)\frac{\partial^4u_i}{\partial x^4}+\frac{h^6}{6!}(2\alpha_1)\frac{\partial^6u_i}{\partial x^6}\\&+\frac{h^8}{8!}(2\alpha_1)\frac{\partial^8u_i}{\partial x^8}+\cdots.\end{aligned} \tag{38}$$

By a term-by-term comparison of the derivatives shown in Eq. (38), the five simultaneous algebraic equations can be derived. The introduced free parameters can then be derived as $\alpha_1=\alpha_{-1}=-1, \alpha_0=2, \beta_0=-1, \gamma_0=-\frac{1}{12}$ and $\delta_0=-\frac{1}{360}$. Note that $w_i=k^3u_i+k^2f_i+k\frac{\partial^2f_i}{\partial x^2}+\frac{\partial^4f_i}{\partial x^4}$, $v_i=k^2u_i+kf_i+\frac{\partial^2f_i}{\partial x^2}$, and $s_i=ku_i+f_i$. Eq. (37) can then be expressed as

$$\begin{aligned}u_{i+1}-\left(2+h^2k+\frac{1}{12}h^4k^2+\frac{1}{360}h^6k^3\right)u_i+u_{i-1}\\=h^2f_i+\frac{1}{12}h^4\left(kf_i+\frac{\partial^2f_i}{\partial x^2}\right)+\frac{1}{360}h^6\left(k^2f_i+k\frac{\partial^2f_i}{\partial x^2}+\frac{\partial^4f_i}{\partial x^4}\right).\end{aligned} \tag{39}$$

The corresponding modified equation for (36) is derived as $\frac{\partial^2u}{\partial x^2}-ku=f+\frac{h^6}{20,160}\frac{\partial^8u}{\partial x^8}+\frac{h^8}{1.814.400}\frac{\partial^{10}u}{\partial x^{10}}+\cdots+H.O.T.$. This means that the proposed three-point scheme is sixth-order accurate.

4. Verification study

The proposed combined compact spatial scheme and pressure correction algorithm will be validated by solving the unsteady Navier–Stokes equations, Leray-α regularized equations, and the NS-α regularized equations. In a square $-1\leqslant x,y\leqslant1$, it is assumed that the exact solutions for the velocity vector $\underline{u}$, filtered velocity vector $\overline{\underline{u}}$, and the scalar pressure p take the following forms provided that the source terms are derived by substituting the solutions of (40)–(44) into their respective equations

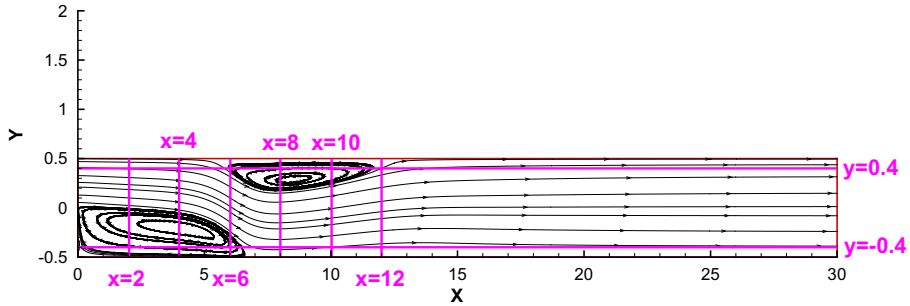

Fig. 13. Illustration of the cutting lines ($x=2,4,6,8,10$ and 12; $y=0.4$ and -0.4) used for the comparison of results in the backward-facing step problem.

$$u(x,y,t) = -cos(\pi x)sin(\pi y)e^{-\frac{2\pi^2 t}{Re}}, \tag{40}$$

$$v(x,y,t) = sin(\pi x)cos(\pi y)e^{-\frac{2\pi^2 t}{Re}}, \tag{41}$$

$$p(x,y,t) = -\frac{1}{4}(cos(2\pi x) + cos(2\pi y))e^{-\frac{4\pi^2 t}{Re}}, \tag{42}$$

$$\overline{u}(x,y) = \cos(\pi x)\cos(\pi y), \tag{43}$$

$$\overline{v}(x,y) = \sin(\pi x)\sin(\pi y). \tag{44}$$

All the calculations will be performed at $Re = 1000$ and $\Delta t = 10^{-2}\Delta x$ for the grid sizes chosen as $\frac{1}{20}, \frac{1}{40}, \frac{1}{80}, \frac{1}{120}, \frac{1}{160}$. In Tables 3–5, one can clearly see that the predicted L_2-norm errors are all fairly small and the computed rates of convergence are high for the Navier–Stokes equations and the regularized equations under current investigation. The proposed discretization scheme and the solution algorithm are thus numerically demonstrated to be correct.

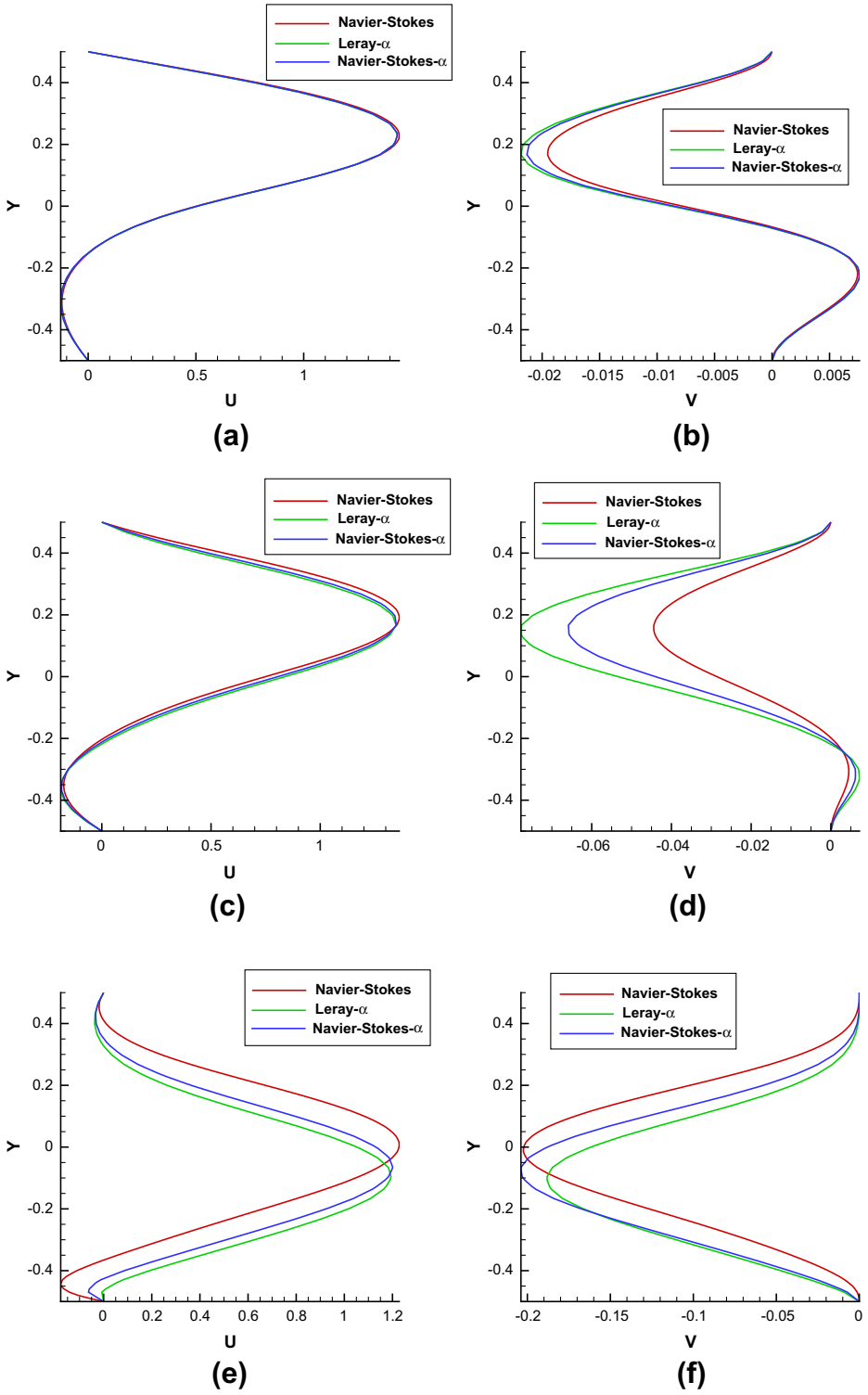

Fig. 14. Comparison of the predicted velocity profiles for the backward-facing step problem. (a) and (b) $x = 2$; (c) and (d) $x = 4$; and (e) and (f) $x = 6$.

Having analytically justifying the proposed numerical method, we will investigate next the lid-driven cavity and the backward-facing step problems to assess the two chosen regularized turbulence models.

5. Discussion of results

We begin with the investigation of the lid-driven cavity flow problem and then the backward-facing step problem. Comparison of our simulated results with other existing reliable results, examination of the zero-divergence condition for the filtered and unfiltered velocity vectors, check on the global mass conservation, and the illustration of the difference of the computed results between the classical and regularized Navier–Stokes equations are the main themes in the following discussion of results.

5.1. Lid-driven cavity problem

The internal flow problem subject to the boundary condition shown in Fig. 1 is considered first. Given the unit upper lid velocity (or $u = 1$), calculation will be performed at $Re = 7500$ in a square of length 1. In this flow simulation, 200×200 mesh points are

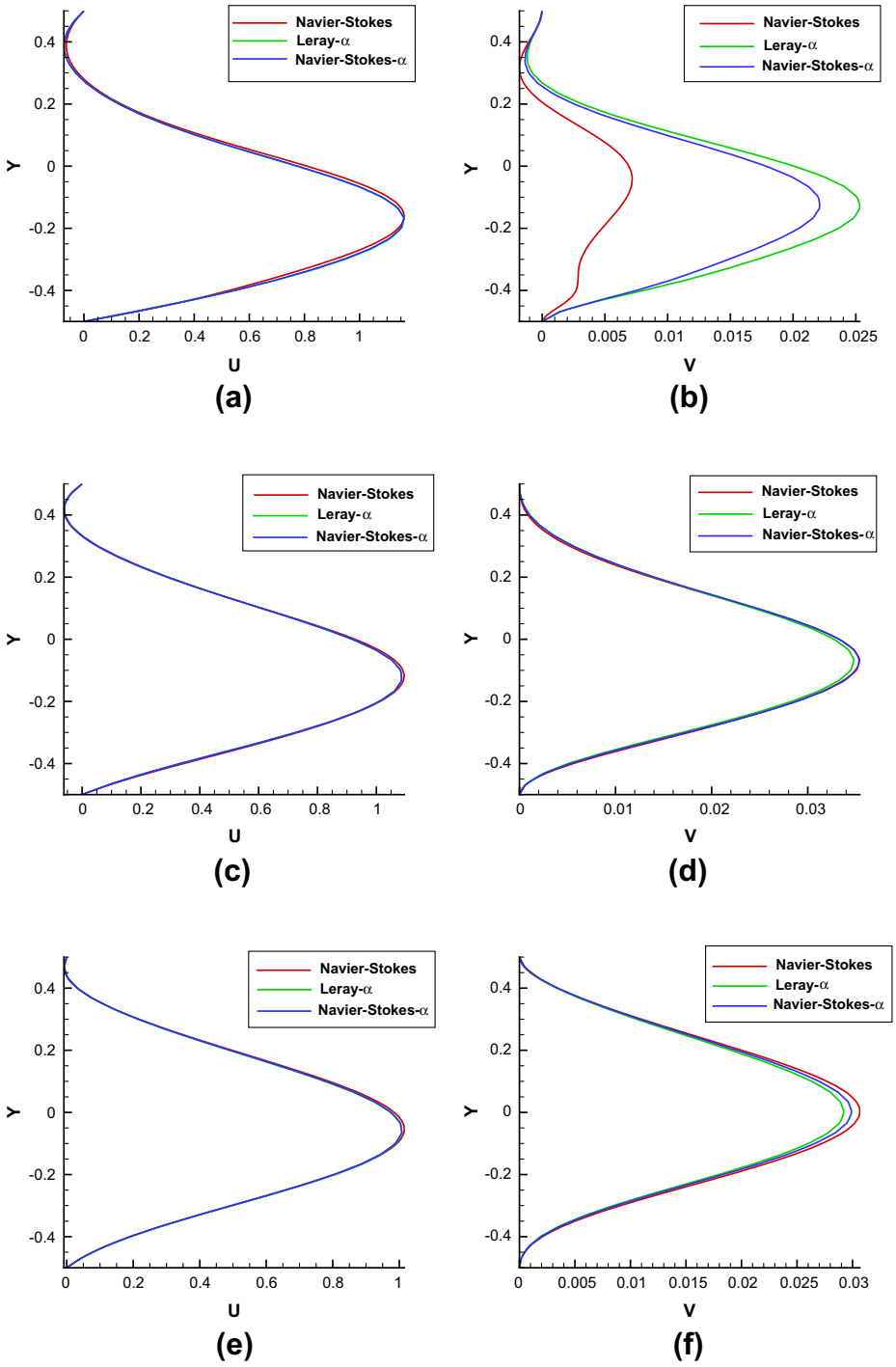

Fig. 15. Comparison of the predicted velocity profiles for the backward-facing step problem. (a) and (b) $x = 8$; (c) and (d) $x = 10$; and (e) and (f) $x = 12$.

uniformly distributed in the square cavity while for the Leray-α and NS-α flow simulations the mesh resolution has been both reduced by four times. In the assessment of the investigated regularization models applied in the domain of 100×100 mesh points, we assume that the NS solutions computed in the finer mesh (200×200 nodal points) are conceptually regarded as being exact.

In Fig. 2, our computed NS velocity profiles at two mid-planes are seen to agree excellently with those of Ghia et al. [23] and Erturk and Corke [24]. It is worthy to point out here that the residual reduction shown in Fig. 3 during the nonlinear iteration is excellent for the two investigated regularization models. This can be considered as an indirect evidence to show the superiority of applying the currently developed advection scheme which accommodates the optimized numerical modified wavenumber. For the comparison sake, the velocity profiles computed from the Leray-α and NS-α equations in the coarser mesh are also plotted in the same figure. One can see that the predicted regularized velocity profiles agree quite well with each other. In comparison, the NS-α velocity profiles are slightly closer to the NS velocity profiles.

We then compare the velocity profiles for u and v along the other five particularly chosen lines illustrated in Fig. 1. These chosen lines pass the central larger eddy and the relatively smaller two corner eddies. In Figs. 4 and 5, the computed differences between the NS and regularized NS velocity profiles appear mainly in the primary eddy. The largest difference occurs near the core of the primary eddy. The corner eddies are found to compare quite well for both sets of the regularization equations. From the viewpoint of the sectional velocity profiles, the NS-α model outperforms the Leray-α model based on the current numerical simulation.

We then check whether or not the value of $\nabla \cdot \underline{u}$ is equal to zero in NS and Leray-α equations and $\nabla \cdot \overline{\underline{u}} = 0$ in the NS-α equations. In this check, the L_2 error norms for $\underline{u}$ and $\overline{\underline{u}}$ are calculated based on the current analysis and we tubulated them in Table 6. One can clearly see from this table that the divergence-free condition is retained for the unfiltered velocity vector $\underline{u}$, or $\nabla \cdot \underline{u} = 0$, for the NS and Leray-α models while it is divergence-free for the filtered velocity, or $\nabla \cdot \overline{\underline{u}} = 0$, only for the NS-α equations. This calculation implies that $\nabla \cdot \underline{u} = \nabla \cdot \overline{\underline{u}} = 0$ cannot be both considered as the governing equations [25,26] in the construction of the regularized turbulent equations subject to the no-slip velocity boundary condition.

The effect of α prescribed for the calculation of the regularized Navier–Stokes equations is also examined. The sectional velocity profiles computed at $a = \frac{1}{100}, \frac{1}{\sqrt{24}}, \frac{1}{2}, \frac{3}{4}$ and $\frac{99}{100}$ in $\alpha(\equiv ah)$, where h denotes the grid size, are plotted in Figs. 6 and 7 for the Leray-α and NS-α equations. It is under our expectation that the regularized Navier–Stokes solutions approach the classical Navier–Stokes solutions as the value of α gradually approaches zero. For the given value of α, a better agreement is found near the wall. The discrepancy becomes increasingly larger in the cavity core with the increased value of α.

Finally, the relative dominance of the convection and diffusion is explored for the cavity flow investigated at $Re = 7500$. Three ratios, which are $R_{NS} = \frac{\underline{u} \cdot \nabla \underline{u}}{\nabla^2 \underline{u}}, R_{Leray-\alpha} = \frac{\overline{\underline{u}} \cdot \nabla \underline{u}}{\nabla^2 \underline{u}}$ and $R_{NS-\alpha} = \frac{\overline{\underline{u}} \cdot \nabla \underline{u}}{\nabla^2 \underline{u}}$, are defined. These results, plotted in Fig. 8 for their contours, show the dominant diffusion phenomenon in the three corner eddies while the convection phenomenon is prevailing in the center eddy. In the upper center eddy, the degree of convection dominance is decreased from the left to the right while in the lower part of the center eddy, the degree of dominance in convection is decreased from right to left. Generally speaking, the smoothing operator

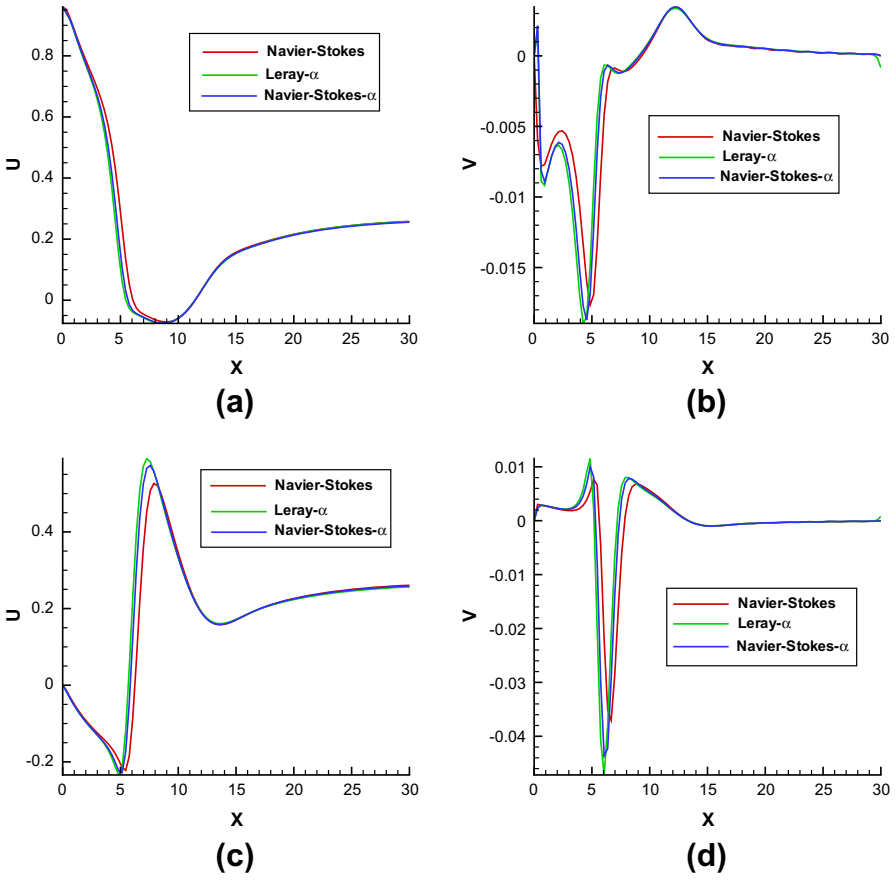

Fig. 16. Comparison of the predicted velocity profiles for the backward-facing step problem. (a) and (b) $y = 0.4$; and (c) and (d) $y = -0.4$.

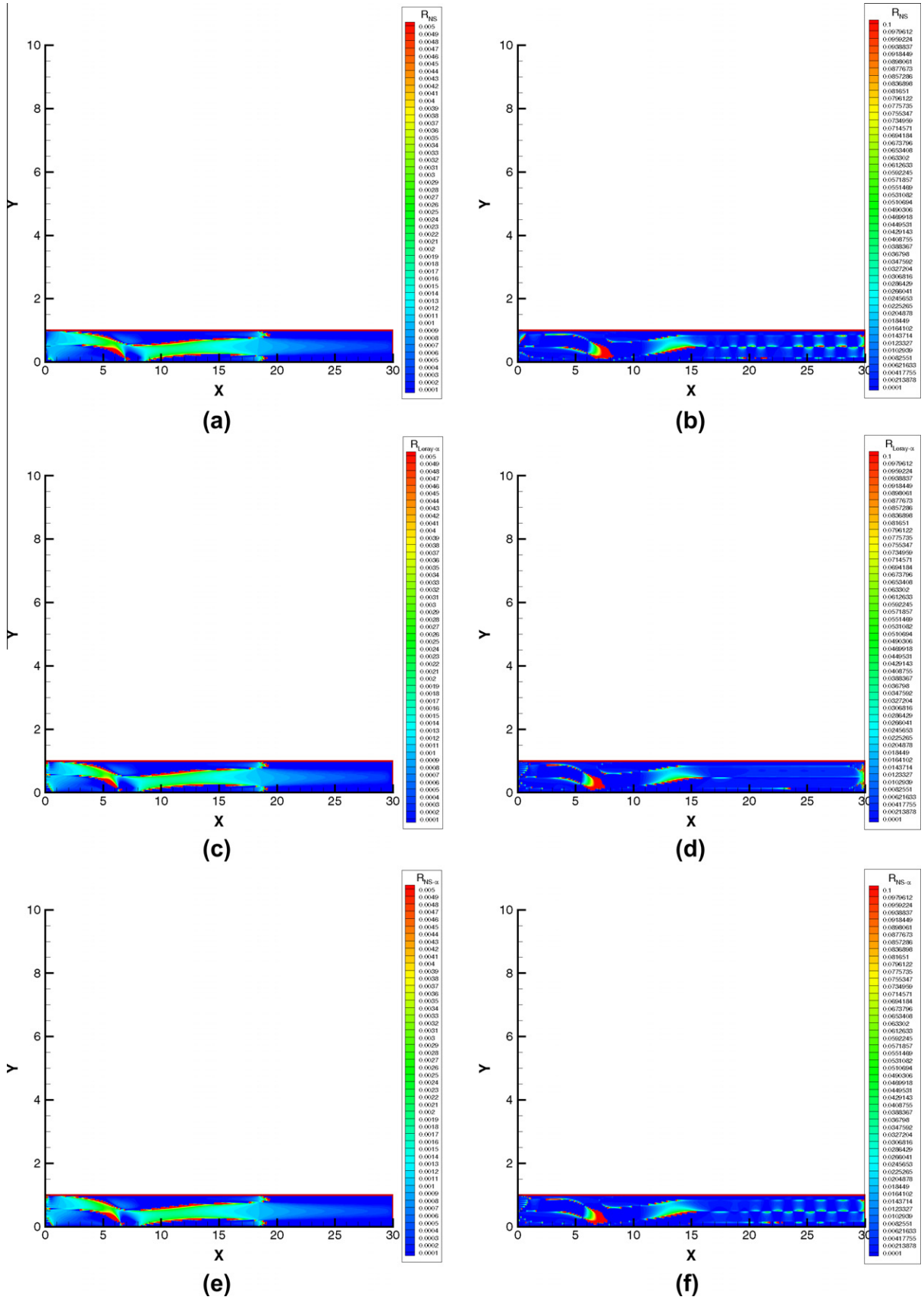

Fig. 17. The computed contours for the backward-facing step problem. (a) R_{NS} for u; (b) R_{NS} for v; (c) $R_{Leray\text{-}\alpha}$ for u; (d) $R_{Leray\text{-}\alpha}$ for v; (e) $R_{NS\text{-}\alpha}$ for u; and (f) $R_{NS\text{-}\alpha}$ for v.

Table 7
The predicted mass fluxes at the lines $x = 3$, 6 and 9 using the two chosen model equations to simulate the backward-facing step problem.

Models	Inlet	$x = 3$	Error (%)	$x = 6$	Error (%)	$x = 9$	Error (%)
Navier–Stokes	0.5	0.500886	0.1773	0.501463	0.2926	0.500981	0.1962
Leray-α	0.5	0.497031	0.5937	0.498299	0.3401	0.497372	0.5254
Navier–Stokes-α	0.5	0.497088	0.5823	0.498810	0.2379	0.497441	0.5116

can regularize the flow in a sense that the distributions of $R_{Leray\text{-}\alpha}$ and $R_{NS\text{-}\alpha}$ become more smooth in comparison with the solution smoothness computed from the classical Navier–Stokes equations.

Table 8
Comparison of the computed divergence errors for $\underline{u}$ from the three sets of equations for solving the backward-facing step problem.

Models	$\nabla \cdot \underline{u}$
Navier–Stokes	1.983×10^{-6}
Leray-α	4.219×10^{-7}
Navier–Stokes-α	4.857×10^{-2}

5.2. Backward-facing step problem

In the current assessment of the regularized Navier–Stokes equations, we investigated also the external flow problem. In this study the well-known benchmark backward-facing step problem schematic in Fig. 9 is considered. In the rectangular domain of the lengths 30 and 1 along the respective x and y directions, the uniform meshes of 1200×60 grid points for the Navier–Stokes equations and 600×30 grid points for the regularized Navier–Stokes equations are considered for the case investigated at $Re = 1000$. Along the inlet, a fully developed velocity vector $(u = 24y(0.5 - y), 0)$ is prescribed while along the outlet the conditions $p = 0$ and $\frac{\partial u}{\partial x} = \frac{\partial v}{\partial x} = 0$ are applied. The rest of the boundaries are specified by $\underline{u} = 0$. As before, the Navier–Stokes solutions computed in the finer

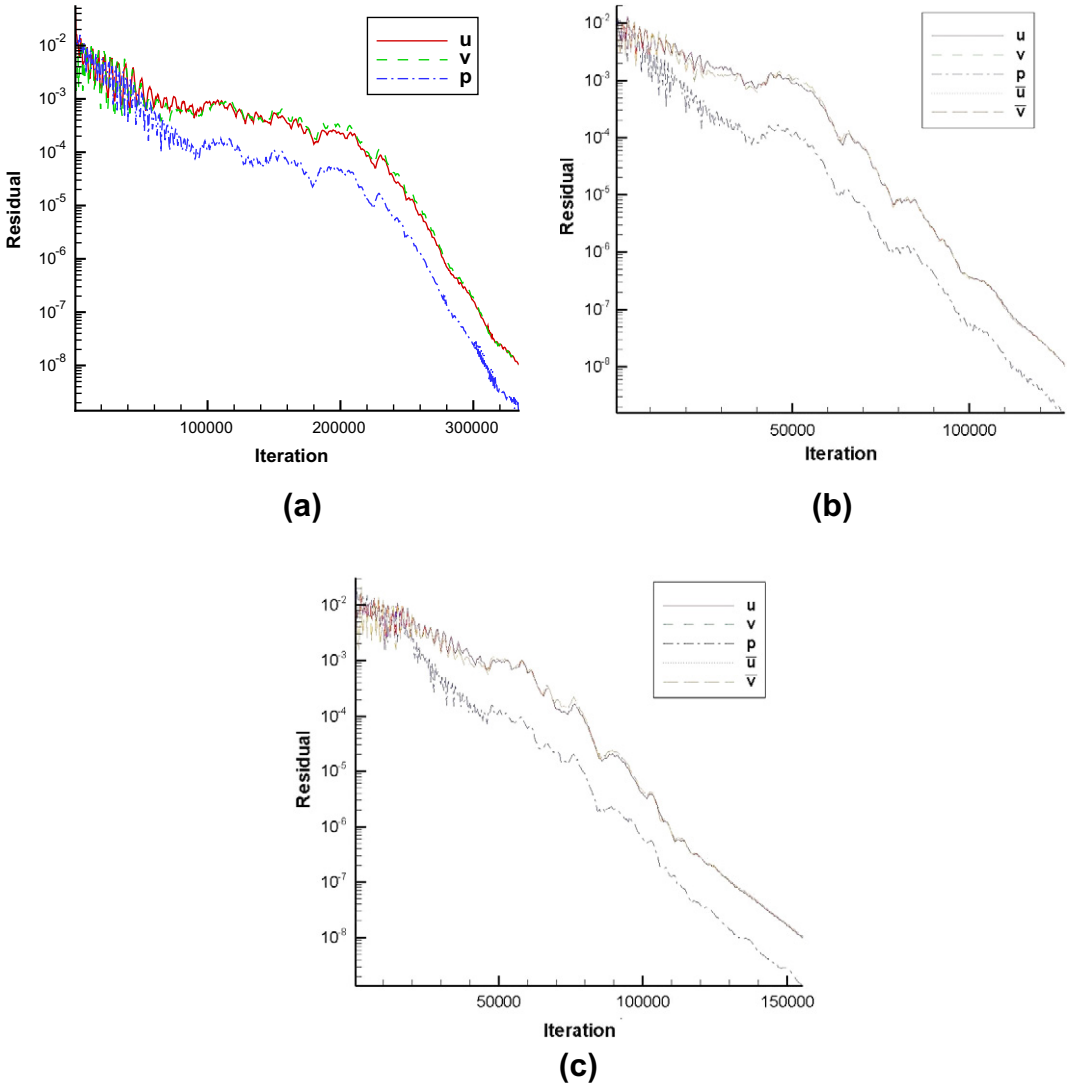

Fig. 18. Illustration of the residual reductions for the backward-facing step problem. (a) Navier–Stokes; (b) Leray-α; and (c) Navier–Stokes-α.

grids are considered as the reference solutions for making the assessment of the regularized turbulence models.

Before the discussion of the computed results, the currently predicted Navier–Stokes solutions will be compared with other available solutions. In Figs. 10–12 good agreement in the velocity profiles and the lengths of the reattachment and separation are seen. These simulated results are considered as the referenced solutions in the later assessment of the regularized solutions.

As in Section 5.1, velocity profiles are plotted at the lines $x = 2, 4, 6, 8, 10, 12$ and $y = 0.04, -0.04$. Except at the outlet, all the lines schematic in Fig. 13 get across the two predicted eddies near the upper and lower channel walls. According to the simulated velocity profiles for $u(y)$ and $v(y)$ in Figs. 14 and 15 and $u(x, 0.4)$ and $v(x, -0.4)$ in Fig. 16, the regularized NS solutions differ from the NS equations mostly in the non-eddy regions. The regularized model solutions agree quite well in the upper and lower eddies. This finding has been also observed in the above lid-driven cavity flow problem. The discrepancy is particularly pronounced at the end of the corner eddy that is attached to the lower channel wall and in the beginning of the roof eddy. This region is, in fact, the most unstable region in the channel. Of the two simulated regularized solution profiles, the NS-α solution has a better agreement with the classical Navier–Stokes solution. This observation is again found as that observed in the lid-driven cavity flow problem. The computed ratios between the convection and diffusion terms defined in Section 5.1 are also plotted in Fig. 17. One can find from these figures that the diffusion effect dominates mostly in the entire channel except in the thin regions located between the free-stream and the upper/lower eddies.

In the current inflow–outflow simulation, it is essential to check whether the predicted sets of solutions accommodate the global mass conservation. For this reason, we integrate the velocity along the cutting lines and tabulate the computed mass in Table 7. One can see that mass is conserved excellently. Also, NS-α model outperforms the Leray-α model since NS-α has a better global mass conservation. We also elaborate on the issue of simultaneously considering $\nabla \cdot \underline{u} = 0$ and $\nabla \cdot \overline{\underline{u}} = 0$ as the governing equations. For this purpose, we plot the L_2 norms of the divergence of the filtered velocity field $\overline{\underline{u}}$ and the unfiltered velocity field in Table 8. As the conclusion made in Section 5.1, only $\nabla \cdot \underline{u} = 0$ holds in the Navier–Stokes and Leray-α equations.

Before closing this section, the excellent convergence of the residuals will be shown using the currently proposed scheme when solving the two chosen sets of Navier–Stokes equations. Quite a monotonic reduction of the residuals can be observed in Fig. 18 for the two investigated regularization equations. The effectiveness of applying the current numerical method is again demonstrated from this inflow–outflow problem.

6. Concluding remarks

In this study a dispersively very accurate convection scheme is proposed to simulate the high Reynolds number flow. Good convergence has been demonstrated due probably to the application of the effective advection scheme which accommodates the optimized numerical wavenumber. Besides the classical Navier–Stokes equations, two types of the regularized Navier–Stokes equations have been numerically studied in details. Of the Leray-α and NS-α subgrid model equations, it can be concluded that the NS-α model is superior to the Leray-α model because the former model yields a better agreement with the classical Navier–Stokes solutions computed in a mesh with four-time grid resolution. The agreement between the classical and regularized Navier–Stokes solutions were all observed in the smaller eddy regions. Larger discrepancy was normally found in the region located between the primary and the corner eddies.

Acknowledgement

This work was supported by the Grants NSC96-2221-E-002-293-MY2, NSC96-2221-E-002-004 and CQSE97R0066-69. The first author would like to thank Prof. Long Lee for his provision of several useful references and fruitful discussion during the current assessment study.

References

[1] Kolmogorov AN. The local structure of turbulence in incompressible viscous fluid for very large Reynolds numbers. Proc R Soc Lond A 1991;434:9–13.
[2] Verstappen R. On restraining the production of small scales of motion in a turbulent channel flow. Comput Fluids 2008;37:887–97.
[3] Pope SB. Turbulent flows. Cambridge: Cambridge University Press; 2000.
[4] Geurts BJ, Kuczaj AK, Titi ES. Regularization modeling for large-eddy simulation of homogeneous isotropic decaying turbulence. J Phys A 2008;41:344008.
[5] Chandy AJ, Frankel SH. Regularization-based sub-grid scale (SGS) models for large eddy simulations (LES) of high-Re decaying isotropic turbulence. J Turbul 2009;10:1–22.
[6] Graham JP, Holm DD, Mininni PD, Pouguet A. Three regularization models of the Navier–Stokes equations. Phys Fluids 2008;20:035107.
[7] Smagorinsky J. General circulation experiments with the primitive equations. Mon Wea Rev 1963;91:99.
[8] Bardina J, Ferziger JC, Reynolds W. Improved subgrid-scale models for large-eddy simulation. Am Inst Aeronaut Astronaut 1980;80:80–1357.
[9] Geurts BJ, Holm DD. Leray and LANS-α modelling of turbulent mixing. J Turbul 2006;7:1–33.
[10] Cheskidov A, Holm DD, Olson E, Titi ES. On a Leray-α model of turbulence. Proc R Soc Lond 2005;461:629–49.
[11] Holm DD, Nadiga BT. Modeling mesoscale turbulence in the barotropic double gyre circulation. J Phys Oceanogr 2003;33:2355–65.
[12] Foias C, Holm DD, Titi ES. The Navier–Stokes-α model of fluid turbulence. Phys D 2001;505:152–3.
[13] Guermond JL, Oden JT, Prudhomme S. An interpretation of the Navier–Stokes-α model as a frame-indifferent Leray regularization. Phys D 2003;177:23–30.
[14] Cheskidov A. Boundary layer for the Navier–Stokes-α model of fluid turbulence. Arch Rat Mech Anal 2004;172:333–62.
[15] Chen S, Holm DD, Margolin LG, Zhang R. Direct numerical simulations of the Navier–Stokes alpha model. Phys D 1999;133:66–83.
[16] Holm DD. Kármán–Howarth theorem for the Lagrangian-averaged Navier–Stokes-α model of turbulence. J Fluid Mech 2002;467:205–14.
[17] Domaradzki JA, Holm DD. Navier–Stokes-alpha model: LES equations with nonlinear dispersion. Eprint arXiv:nlin/0103036; 2001.
[18] Holm DD, Marsden JE, Ratiu TS. The *Euler—Poincare'* equations in geophysical fluid dynamics. In: Proceedings of the ISAAC Newton institute programme in the mathematics of atmospheric and ocean dynamics 2002; 2002.
[19] Graham JP, Holm DD, Mininni PD, Pouguet A. Highly turbulent solutions of the Lagrangian-averaged Navier–Stokes-α model and their large-eddy-simulation potential. Phys Rev E 2007;76:056310.
[20] Tam CKW, Webb JC. Dispersion–relation-preserving finite difference schemes for computational acoustics. J Comput Phys 1993;107:262–81.
[21] Sheu TWH, Chiu PH. A divergence-free-condition compensated method for incompressible Navier–Stokes equations. Comput Meth Appl Mech Eng 2007;196:4479–94.
[22] Sheu TWH, Chen CF, Hsieh LW. Development of a three-point sixth-order compact Helmholtz scheme for scattering wave propagation. J Comput Acoust 2008;16(2):1–17.
[23] Ghia U, Ghia KN, Shin CT. High-Re solutions for incompressible flow using the Navier–Stokes equations and a multigrid method. J Comput Phys 1982;48:387–411.
[24] Erturk E, Corke TC. Numerical solutions of 2-D steady incompressible driven cavity flow at high Reynolds numbers. Int J Numer Meth Fluids 2005;48:747–74.
[25] Olson E, Titi ES. Viscosity versus vorticity stretching: Global well-posedness for a family of Navier–Stokes-α-like models. Nonlin Anal 2007;66:2427–58.
[26] Lunasin E, Kurien S, Titi ES. Spectral scaling of the Leray-α model for two-dimensional turbulence. J Phys A 2007;41:344014.
[27] Ilyin AA, Lunasin EM, Titi ES. A modified-Leray-α subgrid scale model of turbulence. Nonlinearity 2006;19:879–97.
[28] Rebholz LG. A family of new, high order NS-α models arising from helicity correction in Leray turbulence models. J Math Anal Appl 2008;342:246–54.
[29] Van Reeuwijk M, Jonker HJJ, Hanjalic K. Leray-α simulations of wall-bounded turbulent flows. Int J Heat Fluid Flow 2009;30:1044–53.
[30] Layton W, Manica CC, Neda M, Rebholz LG. Numerical analysis and computational comparisons of the NS-α and NS-ω regularizations. Comput Meth Appl Mech Eng 2010;199:916–31.